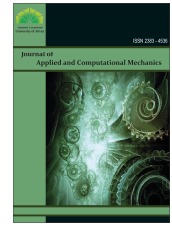




Shahid Chamran  
University of Ahvaz

# Journal of Applied and Computational Mechanics



Research Paper

## Musculoskeletal Modeling and Control of the Human Upper Limb during Manual Wheelchair Propulsion: Application in Functional Electrical Stimulation Rehabilitation Therapy

Mohammad Mahdi Rusta<sup>1</sup>, Seyyed Arash Haghpanah<sup>1</sup>, Sajjad Taghvaei<sup>1</sup>

Department of Mechanical Engineering, Shiraz University, Shiraz, 71936-16548, Iran,  
Email: momarusta@gmail.com (M.M.R.); haghpanah@shirazu.ac.ir (S.A.H.); sj.taghvaei@shirazu.ac.ir (S.T)

Received August 02 2023; Revised September 22 2023; Accepted for publication September 25 2023.

Corresponding author: S.A. Haghpanah (haghpanah@shirazu.ac.ir)

© 2023 Published by Shahid Chamran University of Ahvaz

**Abstract.** Manual wheelchair users rely on their upper limbs for independence and daily activities. The high incidence of upper limb injuries can be attributed to the significant muscular demands imposed by propulsion as a repetitive movement. People with spinal cord injury are at high risk for upper limb injuries, including neuromusculoskeletal pathologies and nociceptive pain, as human upper limbs are poorly designed to facilitate chronic weight-bearing activities, such as manual wheelchair propulsion. Comprehending the underlying biomechanical mechanisms of motor control and developing appropriate rehabilitation tasks are essential to deal with the effects of poor motor control on the performance of manual wheelchair users and prevent long-term upper limb disability, which can interrupt electrical signals between the brain and muscles. Functional electrical stimulation utilizes low-intensity electrical signals to artificially generate body movements by stimulating the damaged peripheral nerves of patients with impaired motor control. Therefore, this study investigates the central nervous system strategy to control human movements, which can be used for task-specific functional electrical stimulation rehabilitation therapy. To this aim, two degrees of freedom musculoskeletal model of the upper limb, including six muscles, is developed, and an optimal controller consisting of two separate optimal parts is proposed to track the desired trajectories in the joint space and estimate the optimal muscle activations regarding physiological constraints. The simulation results are validated with electromyography datasets collected from twelve participants. This study's primary advantages are generating optimal joint torques, accurate trajectory tracking, and good similarities between estimated and measured muscle activations.

**Keywords:** Musculoskeletal modeling, Nonlinear model predictive controller, Static optimization, Manual wheelchair propulsion, Functional electrical stimulation.

### 1. Introduction

Manual wheelchairs (MWs) are typically used assistive devices for people with paraplegia, with over 90% of the approximately 65 million manual wheelchair users (MWUs) worldwide relying on various MWs for mobility [1]. However, the repetitive movements during manual wheelchair propulsion (MWP) can impose excessive loads on the upper limb, leading to low efficiency of the muscle function over time. The high muscle demand can reduce the quality of life (overall health) of manual wheelchair users (MWUs) and make them particularly susceptible to the resulting musculoskeletal pain [2, 3]. Therefore, MWUs are always prone to upper limb pathology and clinical rehabilitation.

Upper limb pain is a common complaint among MWUs, with up to 70% reporting discomfort in the shoulder and wrist joints [4]. From clinical research, even those who do not report pain experience destructive changes in their joints (especially in the shoulder joint) that indicate the possibility of future pain [5]. Upper limb disabilities arising from musculoskeletal injury and pain can significantly prevent MWUs from performing motor activities and stabilizing desired movements, which leads to increased healthcare costs and risks of secondary diseases [6]. Furthermore, people with spinal cord injury (SCI) are at high risk for upper limb joint injuries, including neuromusculoskeletal pathologies and nociceptive pain, as human upper limbs are poorly designed to facilitate chronic weight-bearing activities, such as MWP [7]. Therefore, comprehending the underlying biomechanical mechanisms of motor control and developing appropriate rehabilitation tasks are essential to deal with the effects of poor motor control on the performance of MWUs during MWP and prevent long-term upper limb disability, which can interrupt electrical signals between the brain and muscles.

In recent years, rehabilitation therapy has witnessed significant advancements in innovative techniques to enhance the functional recovery of individuals with musculoskeletal impairments. Among these, Functional Electrical Stimulation (FES) has emerged as a prominent intervention, offering a unique approach to neuromuscular rehabilitation by employing electrical impulses



to activate paralyzed or weakened muscles [8]. While FES holds great promise, it is essential to acknowledge that it is just one facet of the multifaceted landscape of rehabilitation techniques [9]. Other approaches, such as robotic-assisted therapy [10], constraint-induced movement therapy (CIMT) [11], virtual reality-based interventions [12], and telerehabilitation platforms [13, 14], have also gained recognition for their ability to improve motor function, restore limb mobility, and enhance the quality of life for individuals facing various musculoskeletal challenges. This paper delves into the musculoskeletal modeling and control of the human upper limb during manual wheelchair propulsion, specifically focusing on its application within the context of FES while acknowledging the broader spectrum of rehabilitation techniques that contribute to the evolving landscape of musculoskeletal rehabilitation.

Medical professionals have embraced FES as the most favored therapy for this type of issue, given the many techniques developed for this purpose [15]. FES, which belongs to the category of neuromuscular electrical stimulations, is a therapeutic intervention that has demonstrated efficacy in addressing a loss of motor function in patients [16]. This technique utilizes low-intensity electrical signals to artificially generate body movements by stimulating the damaged peripheral nerves of patients with impaired motor control, such as SCI and stroke [17]. When utilizing FES on patients, it has been observed that applying distinct electrical currents, characterized by varying numbers and intensities, elicits a wide array of outcomes [18]. Many researchers have investigated the central nervous system (CNS) strategy to control human movements for task-specific FES rehabilitation therapy, aiming for high accuracy [19-22]. Their reports indicate that motor control could enhance the recovery of upper limb movements through stimulation associated with voluntary attempts. Therefore, the intelligent and efficacious activation of the FES device to stimulate appropriate electrical signals has attracted the attention of scholarly investigations.

However, human movements are performed through the dynamic interactions of the nervous, muscular, and skeletal systems. Nonlinear control structures are frequently utilized to deal with the nonlinearity of these dynamic interactions. Therefore, due to the high redundancy of upper limb musculoskeletal (MSK) models, these control structures are employed to simulate the function of the human CNS in generating the required joint torques-muscle forces during various upper limb movements. In summary, in cases where the CNS or other body organs are injured, such as paralysis or amputation, the motor nervous system (MNS) may weaken, leading to impaired performance. To this aim, since tuning the intensity of electrical stimulation is imperative to perform the desired rehabilitation tasks, human MSK modeling and optimal control of desired joint-task trajectories are the foundations of this field.

In the last decade, bio-inspired MSK models with various degrees of freedom (DOFs) and muscle groups have been presented to simulate the human upper limb movements during rehabilitation tasks, sports exercises, reaching movements, etc. The most widely used MSK models of the upper limb are as follows. Uno et al. [23] were the first researchers to develop a human arm model, which enabled a comprehensive analysis of its biomechanical parameters and established the theoretical foundations for controlling arm reaching movements. Jagodnik and van den Bogert [24] proposed a two DOFs MSK model that approximated a human arm constrained to regulate the desired joint angles in the sagittal plane with no gravity. Zadavec and Matjačić [25] modeled a two DOFs human arm that included the upper arm, forearm, and hand (the forearm and the hand are considered as integrity) to find the optimal trajectories for planar arm reaching movements. The proposed MSK model also consisted of six skeletal muscles (four monoarticular and two biarticular muscles). Since their study aimed to simulate the planar arm reaching movement, it did not contain the gravitational vector. In another study, Sharifi et al. [26] investigated the optimal performance of a two DOFs nonlinear MSK arm model during planar reaching movements. In their proposed MSK model, the shoulder and elbow joints were actuated by the contraction of six muscles. Since robots are popular rehabilitation devices due to their ability to reduce therapist workload and associated costs, Ghannadi et al. [27] developed a rehabilitation robot to promote the rehabilitation of stroke patients. Hence, they modeled a planar two DOFs linkage as a MSK human arm with six muscles. As there was limited available theoretical analysis on the advantages of MSK systems, Wu et al. [28] established a simplified two DOFs four-muscle MSK model to analyze and prove the anti-interference of a MSK system mathematically and experimentally. In their study, the typical movements of the human arm, such as carrying and lifting, are simulated. They considered shoulder and elbow joints, while only two monoarticular muscles actuate each in a vertical two-dimensional plane. As previously explained, MSK pain and disability of the upper limb (especially in the shoulder joint) are the leading causes of designing and developing rehabilitation devices. For this purpose, Ghorbani et al. [29] studied the MSK model and simulation of human arm rehabilitation by a shoulder wheel device in the sagittal plane (without considering contact forces). In another study, Zhao et al. [30] developed a MSK arm model considering the human arm's biomechanical structure and the effects of muscles and skeletons. Their MSK model consisted of two skeletal links (upper arm and forearm) and seven skeletal muscles as the main activated muscles during the planar arm reaching movements.

Coupled equations, nonlinear dynamics, high redundancy in muscle-joint space, and establishing a precise mathematical relationship between joint, muscle, and task spaces are some of the complexities of controlling and simulating MSK models. Furthermore, the control of these bio-inspired MSK models required optimal and accurate control structures. Therefore, numerous model-based control structures have been proposed to deal with the complexity of the MSK models and biomechanical analysis of the various upper limb movements during rehabilitation tasks, sports exercises, daily activities, reaching movements, etc. However, the most relevant studies have been conducted to control and find the optimal trajectories in the task space.

Tahara and Kino [31] proposed an iterative learning control method for a redundant MSK arm model, which could obtain a desired trajectory in the task space with a sufficient internal force. This control structure utilized only muscular space variables, such as muscle length and contractile velocity. Furthermore, they employed another approach to design an iterative learning control method, which utilized multiple space variables from the muscular, joint, and task spaces to improve performance and robustness [32]. Zadavec and Matjacic [25] used an optimal control model based on human arm dynamics, which allowed them to incorporate muscle functioning constraints to find the optimal trajectories for planar arm reaching movements. They evaluated the ability of the minimum joint torque cost function to replicate the trajectories obtained in previously published experimental trials.

The conventional control methods are constrained in handling MIMO-coupled and time-varying systems such as the human MSK arm systems. In contrast, as an adaptive approach, neural network simulations are advantageous for handling these complex dynamics because they provide generalized approximations and adapt to changing conditions. To this end, Wang and Song [33] proposed an adaptive neural fuzzy inference system disturbance observer-based strategy to achieve point-to-point control and trajectory tracking of the end-point of the MSK arm model. In another study, Vatankhah et al. [34] designed an adaptive optimal multi-critic based neuro-fuzzy (AOMCNFC) controller to track the end-point of the multi-input multi-output (MIMO) MSK arm model, which Zadavec and Matjačić previously modeled in [25]. They proposed a separate AOMCNFC control structure based on Takagi-Sugeno-Kang (TSK) fuzzy inference system for each muscle force as a control input. Calculating the real-time optimized muscle force was a significant feature of the proposed controller due to its utility in stimulating the peripheral nerves of the disabled limbs in the field of FES.

Based on the nonlinear controller literature, many studies on upper limb control have used a variety of sliding mode control (SMC) structures due to their real-time response and robustness against uncertainty and external disturbances. For instance, Ghorbani et al. [29] provided an adaptive nonsingular fast terminal sliding mode controller to track the end-point or the human arm during the rehabilitation task with the shoulder wheel device. In another study, Xiuxiang et al. [35] proposed an adaptive fuzzy



sliding mode control method as an angle tracking control of the elbow joint and the end-point of the human MSK. Since each conventional and modern control method has its advantage in dealing with the complexity of the MSK arm model, Zhao et al. [30] compounded the proportional-derivative controller and the two intelligent control methods as an integrated robust controller for assisting arm reaching movements.

Although many studies have examined control strategies for rehabilitation tasks, a few researchers have used optimal control theories like Ghannadi et al. [27]. Their study demonstrated that constant impedance control gains are insufficient for optimal rehabilitation robot performance using a feedback linearization approach. Therefore, they developed a control structure for a two DOFs upper limb stroke rehabilitation robot that assigns optimal impedance gains at each robot configuration during a desired task. Their experimental results demonstrated that the rehabilitation system with the proposed optimal control structure assists more in active-assist therapy while resisting in active-constrained cases. As another implementation of the optimal control on the MSK arm, Sharifi et al. [26] investigated the optimal performance of the planar MSK arm model during reaching movements using an optimal control theory. They considered the summation of two main biomechanical factors (as an optimal objective function): the total time of movement and quadratic function muscle stresses.

Using the MSK model and simulation methods, it is possible to estimate various movement-related variables, such as muscle activations, external forces, and system states. These variables are often difficult to measure through human experiments due to the discomfort that participants experience with painful methods such as indwelling electromyography (EMG) and tendon buckle transducers. Numerous experimental studies have examined the comparative effects of variations in MSK model parameters on the outcome of simulations [36, 37]. According to recent studies, discrepancies in the definitions of joint and segment coordinate systems and disparities in muscle parameters among various MSK models significantly affect simulated joint biomechanics and muscle function [38]. In addition to MSK modeling, a proper optimization method is required to estimate muscle activations due to the high redundancy between the vector of net joint torques and the vector of muscle forces. Static optimization (SO) [39] and computed muscle control (CMC) [40] are the two widely used optimization methods. The SO method is the process of resolving redundancy between joint torques and individual muscle forces using the existing kinematic states of the MSK model (at each time step) and considering the minimization of the desired objective function. In contrast, the CMC method determines muscle excitation by solving a SO to achieve the desired accelerations to track the experimental trajectory. While SO uses the measured accelerations as desired, CMC incorporates a proportional-derivative control structure to reduce errors between the MSK model states and the measured kinematics [39, 40]. Several investigations have compared the estimated muscle activation (EMAs) using SO and CMC [41-46]. It has been proposed that SO is a more robust optimization method for estimating muscle activation during human movements due to its computational efficiency [45, 46]. However, regarding accuracy, the CMC method is superior to the SO method for generating inverse dynamics joint torques [41].

Despite the importance of the MSK model, the validation of the obtained muscle forces/activations through the proposed controllers and the analyses of the various upper limb movements still need to be improved. According to the literature on modeling and control of upper limb MSK models, the proposed control approaches have aimed to control and estimate the optimal trajectories during the various reaching movements in the task space. While in this research, a reliable and optimal control method is required for two aims: generate the optimal low-intensity electrical signals and accurately track the angular positions in the joint space. Note that due to the weak performance of classic optimization algorithms, such as the steepest descent algorithm used in [34], being stuck in local extremum values is the disadvantage of such control structures. In addition, the similarity between EMAs and measured muscle activations (MMAs) is a significant indicator to analyze the performance of control policy, which previous investigations cannot fulfill. Therefore, this experimental study proposes an optimal nonlinear model predictive controller (NMPC) consisting of two separate optimal parts to improve trajectory tracking of measured angular positions in the joint space and estimate the optimal muscle activations regarding physiological constraints. NMPC is the main part of this optimal control structure, which can generate optimal joint torques for accurate trajectory tracking [47]. This optimal control scheme adopts a more robust strategy in dealing with nonlinear dynamics than the CMC's linear control structure. The Levenberg-Marquardt algorithm is used as an iterative algorithm to solve the optimization problem and estimate the optimal joint torques [48]. Note that the superiority of this part is the possibility of considering the allowable range of upper limb joint torques as control constraints. The second part aims to estimate the optimal muscle forces concerning the required joint torques obtained in the first part. Due to the high redundancy of the muscle-joint space and the allowable range of muscle tensile forces, the interior-point-convex quadratic programming (IPCQP) algorithm is used for static optimization [49]. The bound and linear constraints are the allowable range of muscle tensile forces and the relation between muscle tensile forces and estimated joint torques, respectively.

This study is the first attempt to propose an optimal control structure and analyze the performance of the MSK model to track the measured joint trajectories during the MWP. Furthermore, the validity and effectiveness of the proposed approach are confirmed by comparing the simulation results with the MMAs. Generally, the current study is conducted from the following main aspects. In the first step, MSK modeling and simulation of the human upper limb movement during MWP in the sagittal plane. Then, proposing an optimal biologically inspired control scheme as the human CNS to accurately track the desired joint trajectories by generating the required muscle activations, which can be used for task-specific FES rehabilitation therapy. Finally, evaluating EMAs with MMAs. The schematic configuration of the proposed system for task-specific FES rehabilitation therapy is illustrated in Fig. 1.

The remainder of this study is organized as follows: materials and methods are given in section 2. In this section, information about participants and experimental protocols, surface electromyography, force setup and upper limb kinematics, data processing, human upper limb MSK modeling, the structure of the proposed controller, muscle optimization, and validation are discussed in detail. Sections 3 and 4 present the simulation results and discussion, respectively. Finally, sections 5 and 6 summarize this study's conclusions and study limitations, respectively.

## 2. Materials and Methods

### 2.1. Participants and Experimental Protocol

Twelve MWUs in the normal weight category volunteered to participate in this study at Shiraz University (in Mechanical Engineering-Applied Design). The participants had an average age of  $26 \pm 3.27$  years, an average height of  $170 \pm 9.12$  cm, and an average weight of  $70 \pm 6.21$  kg. They could continuously propel the MWs without medical restrictions. None of the participants had upper limb pain, injuries, or disorders that could influence MWP. It is worth noting that all participants were right upper limb dominant, and thus, the required dataset was recorded solely from the right side of their upper limb segments. The Participants received a detailed explanation about the investigation before participating in this research and signed consent forms approved by the Shiraz University ethics committee (No: 9731204).



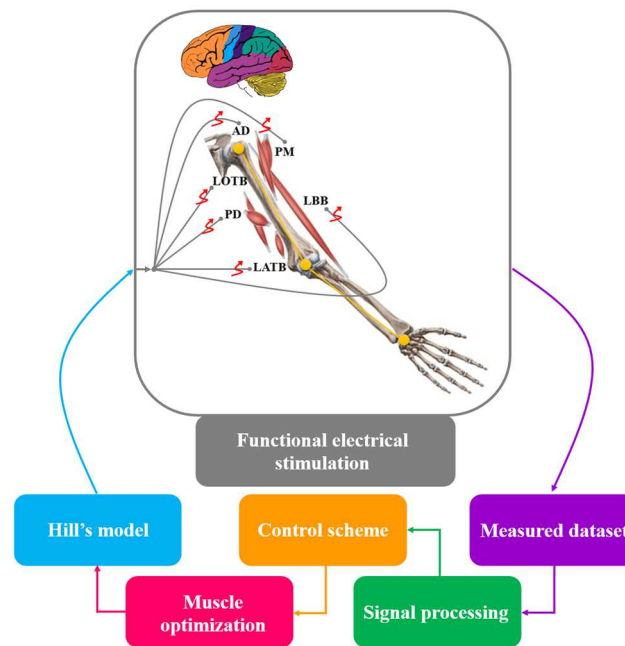


Fig. 1. The schematic configuration of the proposed system for task-specific FES rehabilitation therapy.

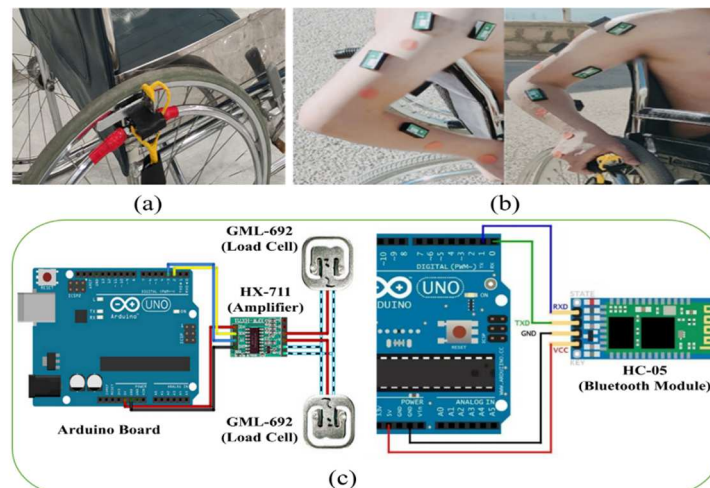


Fig. 2. Designed force sensor system: (a) Mounted ALFS system on pushrim, (b) Placement of the sEMG electrodes on the upper limb muscles, (c) Electrical circuit of ALFS system.

Before the examination, the participants were acquainted with the field test and the study's objectives. The test items were presented to the participants in a procedural format, whereby a semicircular pattern was utilized as the most effective propulsion pattern [50]. The participants were instructed to exert force on both pushrims simultaneously, perform more than twenty propulsion cycles, and propel in a straight line.

## 2.2. Surface Electromyography

In this study, the DataLink software and hardware of Biometrics Ltd. (UK) were employed to record muscle activations. The electrical muscle activities were recorded using wireless surface electromyography (sEMG) sensor (Model: LE230 sEMG sensor; Make: Biometrics Ltd. UK) and data acquisition interface (Model: PIONEER; Make: Biometrics Ltd. UK). Progressive frequency hopping, error detection, data recovery, and high amplifier impedance are among the features of this system.

sEMG dataset was recorded from the following six muscles: anterior deltoid (AD), posterior deltoid (PD), pectoralis major (PM), long head of biceps brachii (LBB), lateral head of triceps brachii (LATB), and long head of triceps brachii (LOTB). Since all participants were right upper limb dominant, the sEMG dataset only recorded from the right upper limb.

Figure 2(b) shows the Surface electrodes placed according to the surface electromyography for the non-invasive assessment of muscles (SENIAM) procedures for skin preparation, placement, fixation, and testing of the sensors [51].

## 2.3. Upper Limb Kinematics

Kinovea software was used to measure the kinematics of the upper limb joints [52, 53]. This low-cost technology is an easy-to-use, portable, and free two-dimensional motion analysis software that allows users to measure and analyze distances, angles, coordinates, and spatiotemporal parameters frame by frame from a recorded video. Several distinct markers were mounted on the anatomical landmarks on the participants' segments, and a high-resolution video camera with a 120 Hz frame rate was used to record the video of the upper limb movements during MWP. It is worth noting that markers must be detectable in all recorded frames.



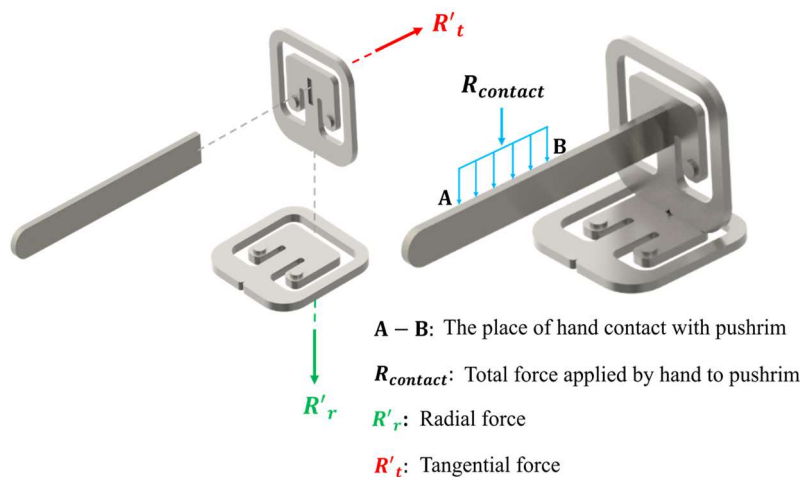


Fig. 3. Designed ALFS system in SolidWorks software.

#### 2.4. Force Setup and Pushrim Force Components

The pushrim force in the sagittal plane consists of two tangential and radial components. An attachable lightweight force sensor (ALFS) system is designed to obtain the values of these components in the push phase. According to the magnitude of the force reported in the review study about MWP [54], butt-welding connection by electric welding is used to create sufficient resistance at the junction of the load cells. A steel lever as shown in Fig. 3 is used to determine the location of the exerted pushrim force, which is connected to the ALFS system. The electrical circuit related to the ALFS system is illustrated in Fig. 2(c). The electrical circuit components include two pairs of load cells (type of GML-692), a pair of analog-to-digital converters (ADC) (type of HX-711), a Bluetooth module (type of HC-05), and an Arduino board (type of UNO).

#### 2.5. Data Processing

The required datasets were recorded from at least twenty complete propulsion cycles. At the beginning of the propulsion, since most of the pushrim force is wasted to overcome friction, a steady state can be reached after two or more consecutive propulsion cycles. Therefore, the first two cycles are neglected, and the subsequent ten cycles for each participant are considered. Note that the push phase started/ended while the pushrim force exerted to the right pushrim is higher/lower than one Nm.

After determining the appropriate cutoff frequency by SENIAM procedures [51], first, the raw sEMG signals were filtered using a fourth-order Butterworth band-pass filter with a selected cutoff frequency (10-500 Hz) and zero phase lag. Then, to perform a proper linear envelope, the filtered sEMG dataset was full-wave rectified and filtered using a fourth-order Butterworth low-pass filter with a cutoff frequency of 6 Hz and zero phase lag [51]. Finally, the processed dataset normalized based on the submaximal method [55, 56]. Pushrim force components were recorded at a frequency of 80 Hz and filtered using a fourth-order Butterworth low-pass filter with a cutoff frequency of 7 Hz and a zero-phase lag [57]. Kinematics dataset was also filtered using a fourth-order Butterworth low-pass filter with a cutoff frequency of 5 Hz and a zero-phase lag [57].

The processed datasets interpolated from zero to 100% using the cubic spline function (with a fixed step size) because the time spent in each cycle varied across participants and propulsion cycles. Then, the average data of ten cycles is calculated for each participant.

#### 2.6. Upper Limb Musculoskeletal Modeling

In this section, the human upper limb is modeled to simulate the upper limb movement during the MWP in the sagittal plane, as shown in Fig. 4. The MSK model includes two DOFs: shoulder flexion-extension and elbow flexion-extension. According to the reports of previous studies and the function of muscles, contraction of AD, PD, PM, LBB, LOTB, and LATB generate the required joint torques for MWP in the sagittal plane [58, 59]. As shown in Fig. 4, the LATB and LBB are bi-articular, and the other muscles are mono-articular. Note that these muscles can only generate tensile forces, and the moment arms of muscles are related to the joint angles.  $L_1$  and  $L_2$  represent the length of the upper arm and forearm, respectively.  $\theta_1$  and  $\theta_2$  represent the relative angular positions of the shoulder and elbow joints, respectively.

The physical parameters of the participants were obtained from the anthropometric data [60]. Table 1 represents the mean of length, mass, and inertia of the upper arm and forearm segments. The physiological cross-sectional area (PCSA) for each muscle was obtained from [61, 62]. The configuration of muscles and the position of their attachments were obtained from [63, 64]. Figure 5 illustrate the insertion and origin points of the muscles.

##### 2.6.1. Kinematics of Muscle-Joint Space

The distance between the insertion and origin points of muscle is defined as muscle length. These lengths  $l_i$  ( $i = 1, \dots, 6$ ) are not constant and are obtained from the following equation:

$$\{l\}_{6 \times 1} = (l_1, l_2, \dots, l_6)^T = \begin{pmatrix} (\check{a}_1^2 + \check{a}_2^2 - 2\check{a}_1\check{a}_2 \sin(\theta_1))^{0.5} \\ (\check{b}_1^2 + \check{b}_2^2 + 2\check{b}_1\check{b}_2 \sin(\theta_1))^{0.5} \\ (\check{c}_1^2 + \check{c}_2^2 - 2\check{c}_1\check{c}_2 \sin(\theta_1))^{0.5} \\ (\check{d}_1^2 + \check{d}_2^2 + L_1^2 - 2\check{d}_1 L_1 \sin(\theta_1) + 2\check{d}_2 L_1 \cos(\theta_2) + 2\check{d}_1 \check{d}_2 \cos(\theta_1 + \theta_2))^{0.5} \\ (\check{e}_1^2 + \check{e}_2^2 + L_1^2 + 2\check{e}_1 L_1 \sin(\theta_1) - 2\check{e}_2 L_1 \cos(\theta_2) + 2\check{e}_1 \check{e}_2 \cos(\theta_1 + \theta_2))^{0.5} \\ (\check{f}_1^2 + \check{f}_2^2 - 2\check{f}_1 \check{f}_2 \cos(\theta_2))^{0.5} \end{pmatrix} \quad (1)$$

where the parameters  $\check{a}_i, \check{b}_i, \check{c}_i, \check{d}_i, \check{e}_i,$  and  $\check{f}_i$  represent the attachment points of AD ( $l_1$ ), PD ( $l_2$ ), PM ( $l_3$ ), LBB ( $l_4$ ), LOTB ( $l_5$ ), and LATB ( $l_6$ ), respectively, as are shown in Fig. 5. The values of these parameters are presented in Table 2.





where arrays ( $w_{ij} \in \mathbb{R}$ ) can be calculated through the partial derivative as follows:

$$w_{ij} = \partial l_j / \partial \theta_i, \quad \begin{cases} i = 1, 2 \\ j = 1, \dots, 6 \end{cases} \quad (4)$$

Based on the principle of virtual work, the joint torques generated from the muscle forces can be obtained as follows:

$$\sum_{j=1}^2 \vec{T}_j \cdot \delta \vec{\theta}_j + \sum_{i=1}^6 \vec{f}_i \cdot \delta \vec{r}_i = 0 \quad (5)$$

$$\{\mathbf{T}\}_{2 \times 1} \{\delta \boldsymbol{\theta}\}_{1 \times 2} + \{\mathbf{F}\}_{6 \times 1} \{\delta \mathbf{l}\}_{1 \times 6} = 0 \quad (6)$$

$$\begin{pmatrix} T_1 \\ T_2 \end{pmatrix} (\delta \theta_1 \quad \delta \theta_2) + \begin{pmatrix} f_1 \\ \vdots \\ f_6 \end{pmatrix} (\delta l_1 \quad \dots \quad \delta l_6) = 0 \quad (7)$$

$$\{\mathbf{T}\}_{2 \times 1} = [-\mathbf{W}(\boldsymbol{\theta})]_{2 \times 6} \{\mathbf{F}\}_{6 \times 1} \quad (8)$$

where  $\{\mathbf{F}\} = (f_1 \dots f_6)^T$  is the vector of muscle tensile forces and  $\{\mathbf{T}\} = (T_1 \ T_2)^T$  is the vector of effective joint torques.

### 2.6.2. Modeling Muscle Dynamics

In this study, the Hill model is used to model the nonlinear behavior of skeletal muscles [65]. The dynamic of muscle based on Hill's force-velocity relationship is as follows:

$$f(\alpha_c, \dot{l}) = p(1 - c\dot{l})\alpha_c - p c_0 \dot{l} \quad (9)$$

where  $c$  and  $p$  are defined as follows:

$$p = 0.9l_0 / (0.9l_0 + |\dot{l}|) \quad (10)$$

$$c = \begin{cases} 0.25/0.9l_0 & \text{if } \dot{l} \geq 0 \\ 2.25/0.9l_0 & \text{if } \dot{l} < 0 \end{cases} \quad (11)$$

and  $f$  is the output force from muscle,  $\dot{l}$  is the muscle contractile velocity, and  $c_0 > 0$  is the muscle intrinsic viscosity. In addition,  $\alpha_c$  is the muscle control input that is defined as follows:

$$\alpha_c = \alpha f_0, \quad 0 \leq \alpha \leq 1 \quad (12)$$

where  $\alpha$  is a muscle activation and  $f_0$  is the maximum output force of the isometric contraction model when the muscle length is intrinsic rest length.

### 2.6.3. Kinematics of Joint-Task Space

The end-point position vector of the skeletal model can be expressed by relative joint angular positions as follows:

$$\{\mathbf{X}\}_{2 \times 1} = (x, y)^T = \begin{pmatrix} +L_1 \sin(\theta_1) + L_2 \sin(\theta_1 + \theta_2) \\ -L_1 \cos(\theta_1) - L_2 \cos(\theta_1 + \theta_2) \end{pmatrix} \quad (13)$$

The time derivative of Eq. (13) is as follows:

$$\{\dot{\mathbf{X}}\}_{2 \times 1} = [\mathbf{J}(\boldsymbol{\theta})]_{2 \times 2} \{\dot{\boldsymbol{\theta}}\}_{2 \times 1} \quad (14)$$

where  $\{\dot{\mathbf{X}}\} \in \mathbb{R}^2$  is the vector of end-point linear velocities and  $[\mathbf{J}(\boldsymbol{\theta})] \in \mathbb{R}^{2 \times 2}$  is the Jacobian matrix from the task space to the joint space which relates the vector of end-point velocities to the vector of joint angular velocities.  $[\mathbf{J}(\boldsymbol{\theta})]_{2 \times 2}$  is determined as follows:

$$[\mathbf{J}(\boldsymbol{\theta})]_{2 \times 2} = \begin{pmatrix} j_{11} & j_{12} \\ j_{21} & j_{22} \end{pmatrix} \quad (15)$$

where arrays are calculated through the partial derivative as follows:

$$\begin{cases} j_{1i} = \partial x / \partial \theta_i \\ j_{2i} = \partial y / \partial \theta_i \end{cases}, \quad i = 1, 2 \quad (16)$$

### 2.6.4. Kinetics of Upper Limb Musculoskeletal Model

In this study, to extract the kinetics of the upper limb during MWP in the sagittal plane, the Lagrange method is used [60]. In this method, the kinetic energy and the potential energy of the entire system should be determined and substituted into the following equation:

$$L = E_k - E_p \quad (17)$$



where  $E_k$  is the kinetic energy of the entire system,  $E_p$  is the potential energy of the entire system, and  $L$  is the Lagrangian. By substituting the Lagrange function in Eq. (18), the Lagrange equation related to the dynamics of the system can be determined through the following equation:

$$\frac{d}{dt} \left( \frac{\partial L}{\partial \dot{q}_k} \right) - \frac{\partial L}{\partial q_k} = Q_{n.c} \quad (18)$$

where  $q_k$  is the generalized coordinate,  $\dot{q}_k$  is the generalized speed, and  $Q_{n.c}$  is the non-conservative force.

The kinetic energy  $E_k$  and potential energy  $E_p$  of the entire system are determined as follows:

$$E_k = \sum_{i=1}^2 \left( \frac{1}{2} m_i (\dot{x}_i^2 + \dot{y}_i^2) + \frac{1}{2} I_i \left( \sum_{j=1}^i \dot{\theta}_j \right)^2 \right) \quad (19)$$

$$E_p = \sum_{i=1}^2 \left( m_i g \left( \sum_{j=1}^{i-1} (L_j (1 - \cos(\sum_{k=1}^j \theta_k))) + d_i (1 - \cos(\sum_{k=1}^i \theta_k)) \right) \right) \quad (20)$$

where  $m_i$ ,  $I_i$ ,  $(x_i, y_i)$ , and  $(\dot{x}_i, \dot{y}_i)$  ( $i = 1, 2$ ) are the mass, moment of inertia, the coordinate of the center of mass, and linear velocity of the center of mass of the upper arm and forearm segments, respectively.  $g$  also is the gravitational acceleration. To calculate the coordinates of the center of mass, the reference coordinate system is considered on the shoulder joint. Therefore, these coordinates are as follows:

$$x_i = \sum_{j=1}^{i-1} (L_j \sin(\sum_{k=1}^j \theta_k)) + d_i \sin(\sum_{k=1}^i \theta_k) \quad (21)$$

$$y_i = \sum_{j=1}^{i-1} (-L_j \cos(\sum_{k=1}^j \theta_k)) - d_i \cos(\sum_{k=1}^i \theta_k) \quad (22)$$

where  $d_i$  ( $i = 1, 2$ ) is the mass center position of the upper arm and forearm segments, respectively. The time derivative of Eqs. (21) and (22) are the linear velocities of the mass center positions that are expressed as follows:

$$\dot{x}_i = \sum_{j=1}^{i-1} (L_j (\sum_{k=1}^j \dot{\theta}_k) \cos(\sum_{k=1}^j \theta_k)) + d_i (\sum_{k=1}^i \dot{\theta}_k) \cos(\sum_{k=1}^i \theta_k) \quad (23)$$

$$\dot{y}_i = \sum_{j=1}^{i-1} (L_j (\sum_{k=1}^j \dot{\theta}_k) \sin(\sum_{k=1}^j \theta_k)) + d_i (\sum_{k=1}^i \dot{\theta}_k) \sin(\sum_{k=1}^i \theta_k) \quad (24)$$

The dynamic equation resulting from the Lagrange method related to the two DOFs skeletal model of the upper limb in the sagittal plane is defined in the form of the following matrix:

$$[\mathbf{M}(\boldsymbol{\theta})]_{2 \times 2} \{\ddot{\boldsymbol{\theta}}\}_{2 \times 1} + [\mathbf{C}(\boldsymbol{\theta}, \dot{\boldsymbol{\theta}})]_{2 \times 2} \{\dot{\boldsymbol{\theta}}\}_{2 \times 1} + \{\mathbf{G}(\boldsymbol{\theta})\}_{2 \times 1} = \{\mathbf{Q}_{n.c}\}_{2 \times 1} \quad (25)$$

where  $[\mathbf{M}(\boldsymbol{\theta})] \in \mathbb{R}^{2 \times 2}$  means the inertia matrix, which is symmetric and positive definite,  $[\mathbf{C}(\boldsymbol{\theta}, \dot{\boldsymbol{\theta}})] \in \mathbb{R}^{2 \times 2}$  means the Coriolis and centrifugal and friction torques matrix, and  $\{\mathbf{G}(\boldsymbol{\theta})\} \in \mathbb{R}^2$  means the gravity vector, which are presented in the Appendix A.  $\{\mathbf{Q}_{n.c}\} \in \mathbb{R}^2$  represents the vector of non-conservative forces which is as follows:

$$\{\mathbf{Q}_{n.c}\}_{2 \times 1} = \{\mathbf{T}\}_{2 \times 1} - \{\boldsymbol{\tau}\}_{2 \times 1} \quad (26)$$

where  $\{\mathbf{T}\} \in \mathbb{R}^2$  means the vector of joint torques generated by the contraction of considered muscles and  $\{\boldsymbol{\tau}\} \in \mathbb{R}^2$  means the vector of external torques that are generated by the reaction of the pushrim force components. Using the principle of virtual work and Eq. (15), the relation between the vector of task space forces and the vector of the joint space torques can be obtained as the following mapping:

$$\{\mathbf{R}_{\mathbf{T}}^T\}_{1 \times 2} \{\delta \mathbf{X}\}_{2 \times 1} = \{\boldsymbol{\tau}^T\}_{1 \times 2} \{\delta \boldsymbol{\theta}\}_{2 \times 1} \quad (27)$$

$$\{\mathbf{R}_{\mathbf{T}}^T\}_{1 \times 2} [\mathbf{J}(\boldsymbol{\theta})]_{2 \times 2} \{\delta \boldsymbol{\theta}\}_{2 \times 1} = \{\boldsymbol{\tau}^T\}_{1 \times 2} \{\delta \boldsymbol{\theta}\}_{2 \times 1} \quad (28)$$

$$\{\boldsymbol{\tau}\}_{2 \times 1} = [\mathbf{J}^T(\boldsymbol{\theta})]_{2 \times 2} \{\mathbf{R}_{\mathbf{T}}\}_{2 \times 1} \quad (29)$$

where  $\{\mathbf{R}_{\mathbf{T}}\} \in \mathbb{R}^2$  is the vector of the horizontal and vertical components of the pushrim force reaction in the task space, which is defined as follows according to Fig. 4:

$$\{\mathbf{R}_{\mathbf{T}}\}_{2 \times 1} = (R_x, R_y)^T \quad (30)$$

$$R_x = R_r \cos(\varphi) - R_t \sin(\varphi) \quad (31)$$



$$R_y = R_r \sin(\varphi) + R_t \cos(\varphi) \tag{32}$$

where  $R_r$  and  $R_t$  are reactions of the radial and tangential components in the task space, respectively. It is worth noting that the magnitudes of the radial and tangential components of the pushrim force are among the available information of the dynamics model measured by the designed force sensor system.

Finally, by integrating the Eqs. (25), (26), and (29) with each other, the following matrix form can be obtained:

$$[\mathbf{M}(\boldsymbol{\theta})]_{2 \times 2} \{\ddot{\boldsymbol{\theta}}\}_{2 \times 1} + \{\mathbf{H}(\boldsymbol{\theta}, \dot{\boldsymbol{\theta}})\}_{2 \times 1} = [-\mathbf{W}(\boldsymbol{\theta})]_{2 \times 6} \{\mathbf{F}\}_{6 \times 1} \tag{33}$$

where  $\{\mathbf{H}(\boldsymbol{\theta}, \dot{\boldsymbol{\theta}})\} \in \mathbb{R}^2$  is defined as follows:

$$\{\mathbf{H}(\boldsymbol{\theta}, \dot{\boldsymbol{\theta}})\}_{2 \times 1} = [\mathbf{C}(\boldsymbol{\theta}, \dot{\boldsymbol{\theta}})]_{2 \times 2} \{\dot{\boldsymbol{\theta}}\}_{2 \times 1} + \{\mathbf{G}(\boldsymbol{\theta})\}_{2 \times 1} + [\mathbf{J}^T(\boldsymbol{\theta})]_{2 \times 2} \{\mathbf{R}_T\}_{2 \times 1} \tag{34}$$

## 2.7. Control Scheme

### 2.7.1. Nonlinear Model Predictive Controller

The extracted dynamic equation of the MSK model is nonlinear, and this section aims to achieve optimal joint torques while accurately tracking the desired angular positions. For this purpose, the nonlinear model predictive controller (NMPC) is used as an optimal control according to the required constraints [47]. The proper objective function  $\mathcal{F}_{JT}$  is defined as follows:

$$\mathcal{F}_{JT} = \sum_{i=1}^2 \sum_{n=0}^{N_p} \left( \hat{\theta}_i(\hat{\mathbf{T}}, t + n\Delta t) - \bar{\theta}_i(t + n\Delta t) \right)^2 = \sum_{i=1}^2 \sum_{n=0}^{N_p} e_i^2(\hat{\mathbf{T}}, t + n\Delta t) \tag{35}$$

where  $\hat{\theta}_i$  and  $\bar{\theta}_i$  ( $i = 1, 2$ ) are the estimated and measured angular positions of the upper arm and forearm segments, respectively.  $\Delta t$  is the time step and  $N_p$  is the prediction horizon.

Since the objective function  $\mathcal{F}_{JT}(\hat{\mathbf{T}}, t)$  is a nonlinear least square function and subjects to bounded constraints, the optimization problem cannot be solved analytically. Therefore, the Levenberg-Marquardt algorithm is used as an iterative algorithm to estimate the optimal joint torques  $\{\hat{\mathbf{T}}(t)\}_{2 \times 1}$  according to the selected objective function  $\mathcal{F}_{JT}(\hat{\mathbf{T}}, t)$  [48].

This algorithm aims to minimize the following nonlinear least square function:

$$\min_{\mathbf{T} \in \mathbb{R}^{2(N_p+1)}} \mathcal{F}_{JT}(\hat{\mathbf{T}}, t) = \sum_{i=1}^2 \sum_{n=0}^{N_p} e_i^2(\hat{\mathbf{T}}, t + n\Delta t) = \sum_{j=1}^{2(N_p+1)} \psi_j^2(\hat{\mathbf{T}}) = \|\boldsymbol{\Psi}(\hat{\mathbf{T}})\|_2^2 \tag{36}$$

where the vector  $\{\boldsymbol{\Psi}(\hat{\mathbf{T}})\} \in \mathbb{R}^{2(N_p+1)}$  is:

$$\boldsymbol{\Psi}(\hat{\mathbf{T}}) = \begin{pmatrix} \psi_1(\hat{\mathbf{T}}) \\ \vdots \\ \psi_j(\hat{\mathbf{T}}) \\ \vdots \\ \psi_{2(N_p+1)}(\hat{\mathbf{T}}) \end{pmatrix} = \begin{pmatrix} e_1^2(\hat{\mathbf{T}}, t) \\ \vdots \\ e_1^2(\hat{\mathbf{T}}, t + N_p\Delta t) \\ e_2^2(\hat{\mathbf{T}}, t) \\ \vdots \\ e_2^2(\hat{\mathbf{T}}, t + N_p\Delta t) \end{pmatrix}. \tag{37}$$

Note that since the aim of defining  $\mathcal{F}_{JT}$  is to minimize the error of trajectory tracking, the residual  $\|\boldsymbol{\Psi}(\hat{\mathbf{T}})\|$  is likely to be small at the optimal position.

However, at each iteration  $it$ , the Levenberg-Marquardt method uses a search direction  $\{\mathbf{D}_{it}\} \in \mathbb{R}^{2(N_p+1)}$  that is a solution of the following linear set of equations:

$$(\boldsymbol{\Gamma}^T(\hat{\mathbf{T}}_{it})\boldsymbol{\Gamma}(\hat{\mathbf{T}}_{it}) + \lambda_{it}\text{diag}(\boldsymbol{\Gamma}^T(\hat{\mathbf{T}}_{it})\boldsymbol{\Gamma}(\hat{\mathbf{T}}_{it})))\mathbf{D}_{it} = -\boldsymbol{\Gamma}^T(\hat{\mathbf{T}}_{it})\boldsymbol{\Psi}(\hat{\mathbf{T}}_{it}) \tag{38}$$

where  $[\boldsymbol{\Gamma}(\hat{\mathbf{T}})] \in \mathbb{R}^{2(N_p+1) \times 2(N_p+1)}$  denotes the Jacobean matrix of  $\boldsymbol{\Psi}(\hat{\mathbf{T}})$  and  $\lambda_m$  controls the magnitude and direction of  $\mathbf{D}_m$ . Note that the Levenberg-Marquardt algorithm uses a search direction that is a cross between the Gauss-Newton direction and the steepest descent direction [66].

In the unconstrained problem, the stopping condition usually defines as follows:

$$\|\nabla \mathcal{F}_{JT}(\hat{\mathbf{T}}, t)\|_{\infty} \leq \varepsilon \tag{39}$$

where  $\varepsilon$  is the optimality tolerance value.

**Remark.** Since the objective function  $\mathcal{F}_{JT}$  subjects to the bound constraints, the Levenberg-Marquardt iterations should be modified. If the vector of optimal joint torques at each iteration  $\hat{\mathbf{T}}_{it}$  lies outside the bounds, the algorithm sets the values equal to the nearest maximum/minimum value of the bounds. The modification operator  $\Omega$  operates on each optimal estimated variable  $\hat{T}_i$  independently according to the following equation:

$$\Omega(\hat{T}_i) = \begin{cases} lb_i & \text{if } \hat{T}_i < lb_i \\ ub_i & \text{if } \hat{T}_i > ub_i \\ \hat{T}_i & \text{otherwise} \end{cases} \tag{40}$$



where  $lb_i$  and  $ub_i$  are the lower and upper bounds of  $i$ th joint torque, respectively. Furthermore, the algorithm modifies the stopping condition for the first-order optimality measure as follows:

$$\|\widehat{\mathbf{T}} - \Omega(\widehat{\mathbf{T}} - \nabla \mathcal{F}_{JT}(\widehat{\mathbf{T}}, t))\|_{\infty}^2 \leq \varepsilon \|\nabla \mathcal{F}_{JT}(\widehat{\mathbf{T}}, t)\|_{\infty}. \quad (41)$$

### 2.7.2. Muscle Optimization

This section aims to obtain the optimal muscle forces  $\{\widehat{\mathbf{F}}(t)\}_{6 \times 1}$  at each time step according to the optimal joint torques  $\{\widehat{\mathbf{T}}^{opt}(t)\}_{2 \times 1}$ , which are obtained by NMPC. Due to the high redundancy of the muscle-joint space (Eq. (8)) and the allowable range of muscle tensile forces, the interior-point-convex quadratic programming (IPCQP) algorithm is used for static optimization [49].

As previously explained, repetitive movements of the upper limb lead to low efficiency of the MWP and increased MSK pains, which affect the quality of life. The primary cause of pain and reduced mobility in MWUs is muscle Stress. Therefore, the following objective function is considered to minimize the error of muscle Stress:

$$\mathcal{F}_{MF}(\widehat{\mathbf{F}}, t) = \frac{1}{2} \sum_{i=1}^6 \hat{f}_i^2. \quad (42)$$

The objective function is subject to some linear and bound constraints that should be considered in the optimization algorithm. Since muscle forces in the MSK system should always be positive and in the range of the maximum isometric tensile force, and there is a relation between muscle forces and joint torques, the linear constraints and bound constraints are considered as follows:

$$\{\widehat{\mathbf{T}}^{opt}\}_{2 \times 1} = [-\mathbf{W}(\boldsymbol{\theta})]_{2 \times 6} \{\widehat{\mathbf{F}}\}_{6 \times 1} \quad (43)$$

$$0 \leq \hat{f}_i \leq \sigma_{max} PCSA_i \quad (44)$$

where  $\sigma_{max}$  is the maximum allowable muscle stress and  $PCSA$  is the physiological cross-sectional area.

The IPCQP algorithm aims to minimize the following quadratic function:

$$\min_{\widehat{\mathbf{F}} \in \mathbb{R}^6} \frac{1}{2} \widehat{\mathbf{F}}^T \mathbf{P} \widehat{\mathbf{F}} + \mathbf{Q}^T \widehat{\mathbf{F}} \quad (45)$$

subject to linear and bound constraints. Therefore, the defined linear square problem should be reformulated as a quadratic form by defining  $\mathbf{P}$  as a unit matrix and  $\mathbf{Q}$  as a zero vector. Finally, the EMAs are calculated by Substituting obtained optimal muscle forces into the Hill model.

The diagram of control scheme is shown in Fig. 6.

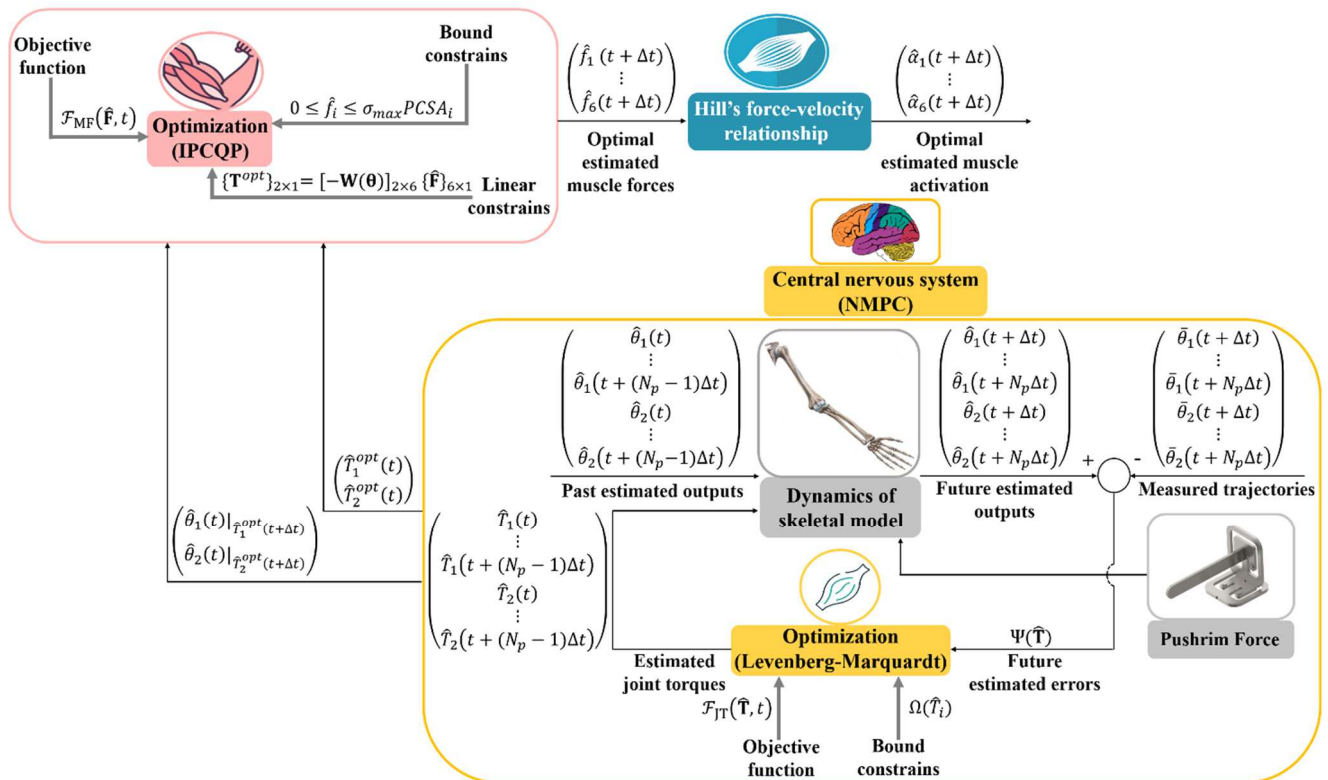


Fig. 6. Diagram of control scheme.



### 2.8. Statistical Analysis

This section aims to compare EMA ( $\hat{\alpha}$ ) and MMA ( $\bar{\alpha}$ ) for validation. Structural similarities between various muscle activations are quantified using Pearson’s correlation coefficient ( $r$ ) [67], which can be obtained as follows:

$$r = \frac{n \sum_i^n \hat{\alpha}_i \bar{\alpha}_i - \sum_i^n \hat{\alpha}_i \sum_i^n \bar{\alpha}_i}{\sqrt{n \sum_i^n \hat{\alpha}_i^2 - (\sum_i^n \hat{\alpha}_i)^2} \sqrt{n \sum_i^n \bar{\alpha}_i^2 - (\sum_i^n \bar{\alpha}_i)^2}} \tag{46}$$

where  $\hat{\alpha}_i$  and  $\bar{\alpha}_i$  are the individual sample points indexed with  $i = 1, \dots, 6$ .

For a positive value of  $r$ , the similarities between muscle activations are classified into three categories, fair, good, and excellent, based on the value of the correlation coefficient (CC) ( $r \leq 0.3$  indicates a fair similarity,  $0.3 < r \leq 0.7$  indicates a good similarity, and  $0.7 < r \leq 1$  indicates an excellent similarity). For a negative value of  $r$ , the dissimilarities between muscle activations are classified into three categories, fair, good, and excellent, based on the CC value ( $r \geq -0.3$  indicates a fair dissimilarity,  $-0.3 > r \geq -0.7$  indicates a good dissimilarity, and  $-0.7 > r \geq -1$  indicates an excellent dissimilarity). Increasing the value of  $r$  means increasing the similarity, and decreasing the value of  $r$  means decreasing the similarity. The probability value (Pvalue) as a level of significance is set at  $p < 0.05$ .

Therefore, the CCs between  $\hat{\alpha}_i$  and  $\bar{\alpha}_i$  are quantified as follows:

$$r = \text{correlation}(\hat{\alpha}_i, \bar{\alpha}_i) \quad , \quad i = 1, \dots, 6 \tag{47}$$

## 3. Results

A custom-written Matlab® program, version R2021b (Mathworks Inc., Natick, MA, USA), processes the dataset, extracts required equations, implements control structure, and performs statistical analysis. The simulation results are presented as follows.

### 3.1. Processed Surface Electromyography

Figure 7 illustrates the processed temporal pattern of muscle activations during MWP. AD and PM are located in the anterior area of the shoulder joint space, and PD is in the posterior area. Therefore, we can consider the AD and PM as agonist muscles during shoulder flexion, whereas the PD act as an antagonist. Since the LATB and LOTB are located in the posterior area, and LBB is located in the anterior area of the elbow joint, we can consider these two muscle groups as the antagonist and agonist muscle groups during elbow flexion, respectively. Note that LOTB and LBB act as biarticular muscles. Therefore, based on these muscles’ insertion and origin points, LBB and LOTB also act as shoulder flexor and shoulder extensor muscles, respectively.

### 3.2. Processed Pushrim Force

In this study, the designed ALFS system was used to measure the pushrim force components in the sagittal plane. Thanks to this designed system, all participants used their own MWs. The validation results of ALFS system (error of the measured forces) are shown in Table 3. In addition, the temporal pattern of tangential and radial components are shown in Fig. 8.

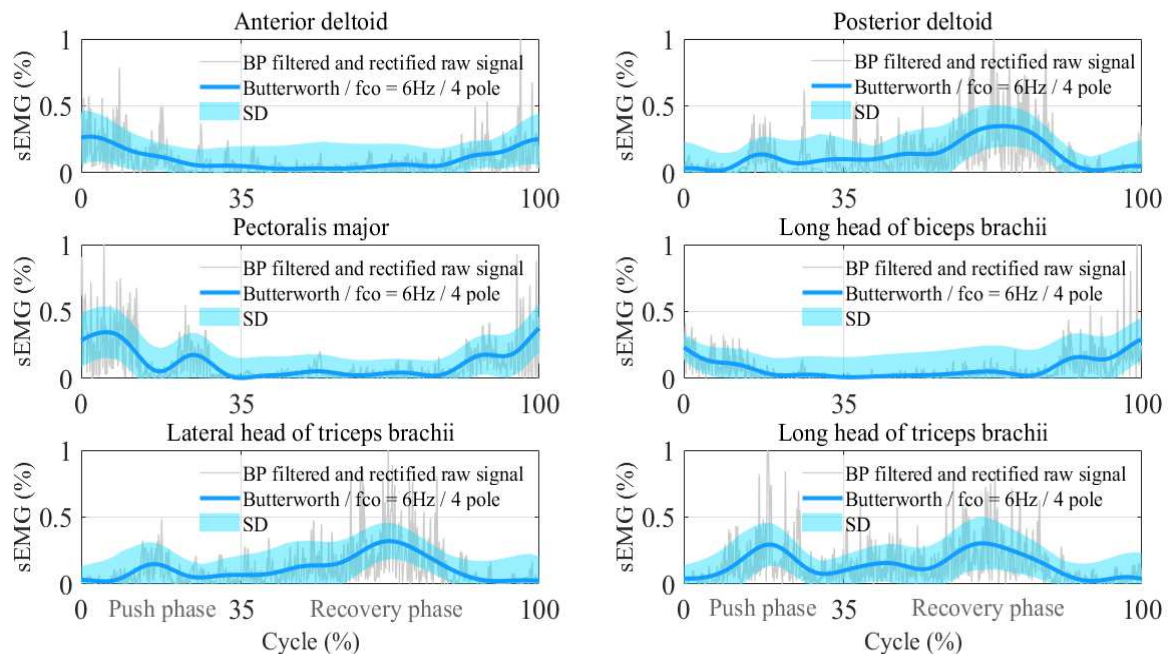


Fig. 7. Processed temporal pattern of MMAs.

Table 3. Calibration results of the ALFS system.

Known	Load (Kg)	5	10	20
	Force (N)	49.05	98.1	196.2
Measured	Force (N)	48.96	97.95	195.96
Error		0.09	0.15	0.24
Mean (SD)		0.16 (0.07)		

∴ Value is mean ± standard deviation



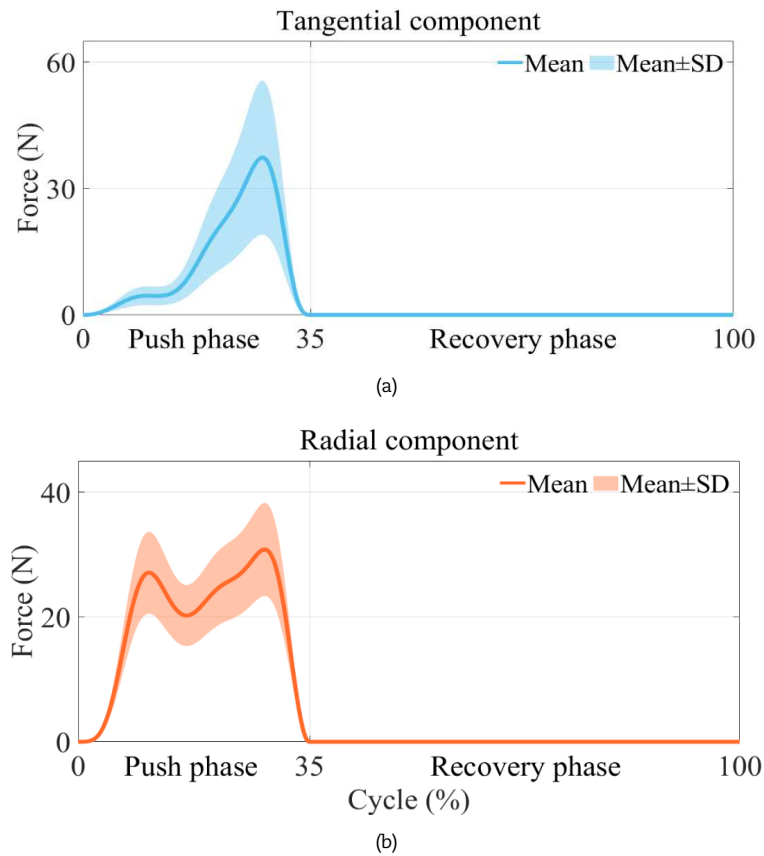


Fig. 8. Pushrim force (SD: standard deviation): (a) Tangential component; (b) Radial component.

The tangential component ( $R_t$ ) is illustrated in a modal curve, which represents a single peak with a value of 39.32 (18.3) N at approximately 72.84% of the push phase. In contrast, the radial component of the pushrim force ( $R_r$ ) is illustrated in a bimodal curve, which represents the first and second peaks at 32.88% and 76.51% of the push phase, respectively. The maximum radial component corresponds to the second peak with a value of 30.8 (7.4) N.

### 3.3. Processed Upper Limb Joints' Kinematics

As the output of the Kinovea software, the kinematic data required to analyze the CNS strategy during MWP in the sagittal plane is shown in Fig. 9, which shows continuous curves of measured kinematic data corresponding to shoulder flexion-extension and elbow flexion-extension.

### 3.4. Results of Nonlinear Model Predictive Controller

Figure 9 shows the results of implementing NMPC including estimated angular positions and the control inputs generated by the controller as the upper limb joint torques. At the beginning of the tracking, the segments of the upper limb are in the initial angular positions of [-0.87 rad, 0.9 rad].

The shoulder and elbow joint torques can be considered bimodal curves because they have two main peaks. The main peak of the shoulder and elbow joint torques corresponds to the last half of the push phase at 30.3% of the propulsion cycle, which have absolute values of 27.1 Nm and 19.1 Nm, respectively.

### 3.5. Results of Muscle Optimization

Figure 10 shows the results of muscle optimization that represents the EMAs. According to the Fig. 10 and muscles' function [51], in the shoulder muscle-joint space, the co-contraction of AD and PM (monoarticular muscles) and the contraction of LBB (biarticular muscle) lead to an increase of  $\theta_1$  (shoulder flexion), while the contraction of PD (monoarticular muscle) and LOTB (biarticular muscle) leads to a decrease of  $\theta_1$  (shoulder extension). In the elbow muscle-joint space, the contraction of LBB leads to an increase of  $\theta_2$  (elbow flexion), while the contraction of LATB (monoarticular muscle) and LOTB leads to a decrease of  $\theta_2$  (elbow extension).

### 3.6. Validation Results

The results obtained from calculating CCs and Pvalues between the EMAs and MMAs are shown in Fig. 11 as color maps. The white cells show the CC value and Pvalue of each EMA/MMA relative to itself, which are the symmetry border of tables. Since the value of CC changes between -1 and 1, this classification makes it possible to identify agonist and antagonist muscles. The correlation results are classified into the following subspaces.

#### 3.6.1. Correlation Coefficients between Measured Muscle Activations

Comparing the CCs between the MMAs of the agonist muscles represents an excellent similarity between  $\bar{\alpha}_{AD}$ ,  $\bar{\alpha}_{PM}$ , and  $\bar{\alpha}_{LBB}$  with the values of  $r \geq 0.7$  ( $p < 0.05$ ). For antagonist muscles, comparing the CCs between the MMAs represents an excellent similarity between  $\bar{\alpha}_{PD}$ ,  $\bar{\alpha}_{LATB}$ , and  $\bar{\alpha}_{LOTB}$  with the values of  $r \geq 0.7$  ( $p < 0.05$ ). Comparing the CCs between the MMAs of the agonist muscles and MMAs of the antagonist muscles represents a good dissimilarity with the values of  $-0.5 > r \geq -0.7$  ( $p < 0.05$ ) between the following muscle pairs:  $(\bar{\alpha}_{AD}, \bar{\alpha}_{LATB})$ ,  $(\bar{\alpha}_{AD}, \bar{\alpha}_{PD})$ ,  $(\bar{\alpha}_{PD}, \bar{\alpha}_{PM})$ ,  $(\bar{\alpha}_{PM}, \bar{\alpha}_{LATB})$ ,  $(\bar{\alpha}_{PM}, \bar{\alpha}_{LOTB})$ , and  $(\bar{\alpha}_{LBB}, \bar{\alpha}_{LOTB})$ .



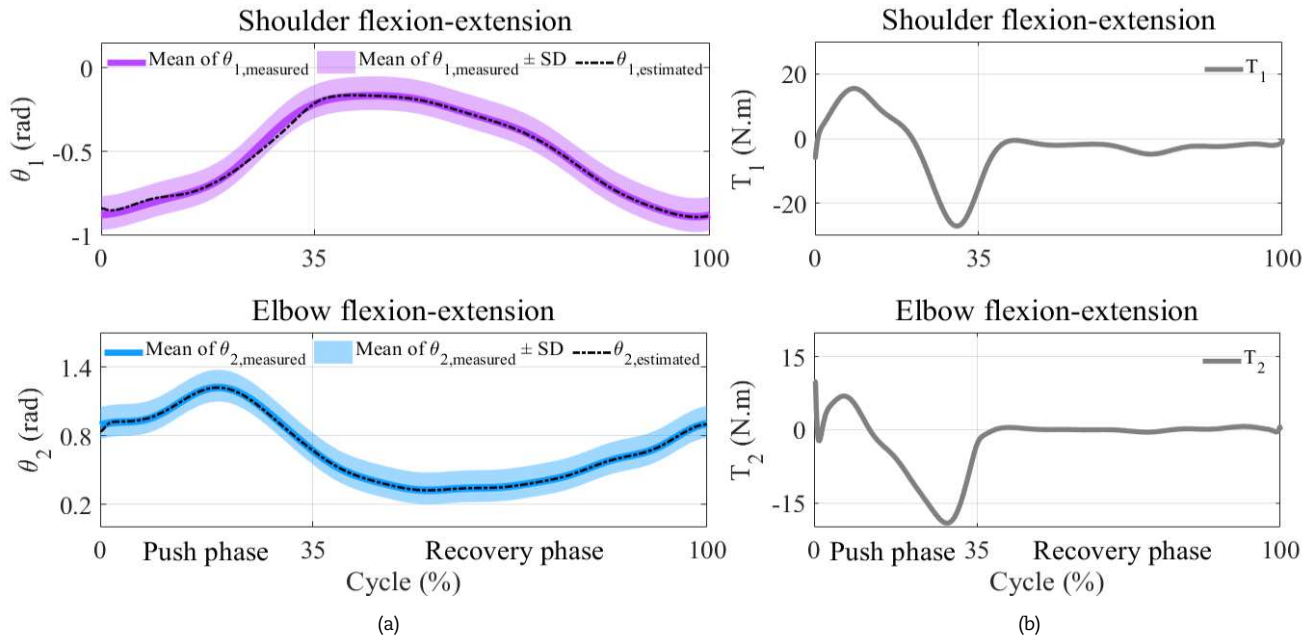


Fig. 9. Simulation results: (a) Trajectory tracking of the measured angular positions; (b) Generated joint torques.

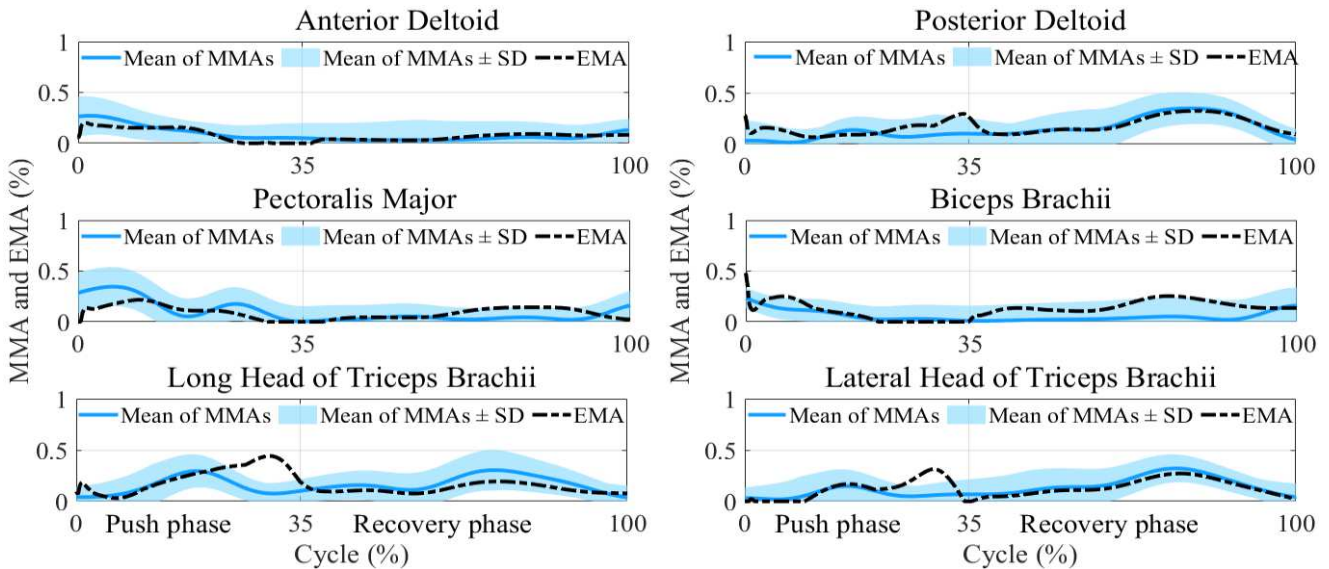


Fig. 10. EMAs and MMAs.

### 3.6.2. Correlation Coefficients between Estimated Muscle Activations

Comparing the CCs between the EMAs of the agonist muscles represents a good similarity with the values of  $0.3 < r \leq 0.7$  ( $p < 0.05$ ) between the following muscle pairs:  $(\hat{\alpha}_{AD}, \hat{\alpha}_{PM})$  and  $(\hat{\alpha}_{PM}, \hat{\alpha}_{LBB})$ . A fair similarity is also obtained between  $\hat{\alpha}_{AD}$  and  $\hat{\alpha}_{LBB}$  with the value of  $r \leq 0.3$  ( $p < 0.05$ ). For antagonist muscles, comparing the CCs between the EMAs represents a good similarity with the values of  $0.3 < r \leq 0.7$  ( $p < 0.05$ ) between the following muscle pairs:  $(\hat{\alpha}_{PD}, \hat{\alpha}_{LATB})$  and  $(\hat{\alpha}_{LOTB}, \hat{\alpha}_{LATB})$ . A fair similarity is also obtained between  $\hat{\alpha}_{PD}$  and  $\hat{\alpha}_{LOTB}$  with the value of  $r \leq 0.3$  ( $p < 0.05$ ). Comparing the CCs between the EMAs of the agonist muscles and EMAs of the antagonist muscles only represents a good dissimilarity with the value of  $-0.5 > r \geq -0.7$  ( $p < 0.05$ ) between  $\hat{\alpha}_{LBB}$  and  $\hat{\alpha}_{LOTB}$ .

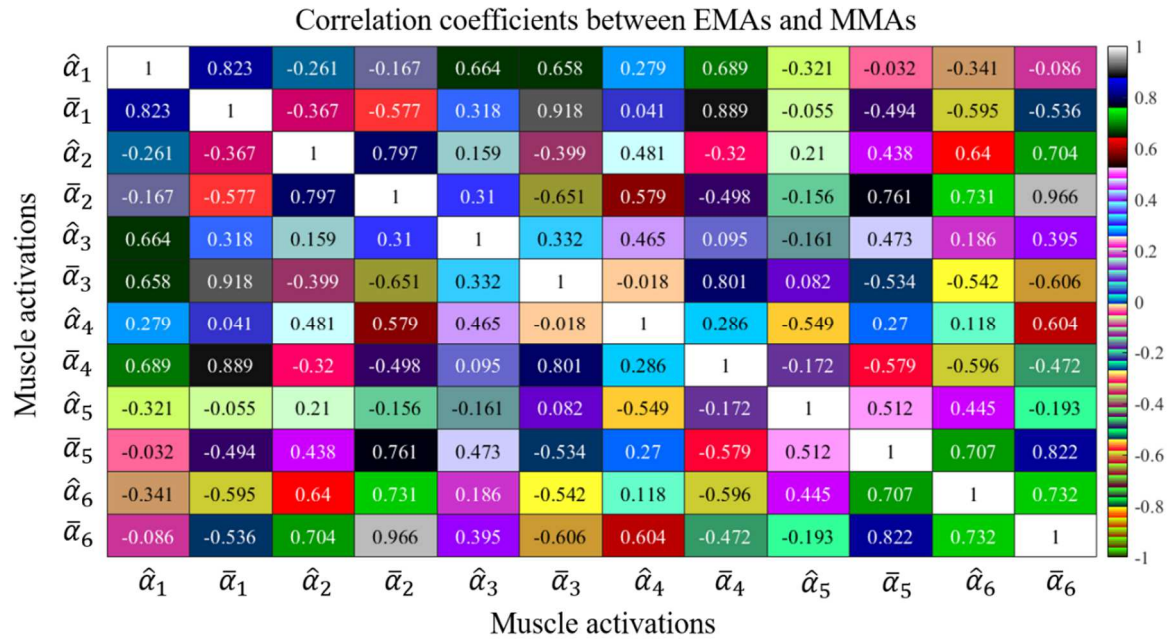
### 3.6.3. Correlation Coefficients between Measured and Estimated Muscle Activations

Comparing the CCs between the EMAs and MMAs represents that the high correlation is between  $\hat{\alpha}_{AD}$  and  $\bar{\alpha}_{AD}$  with a value of  $r = 0.823$  ( $p < 0.05$ ), which indicates an excellent similarity. The lowest correlation is between  $\hat{\alpha}_{LBB}$  and  $\bar{\alpha}_{LBB}$  with a value of  $r = 0.286$  ( $p < 0.05$ ), which indicates a fair similarity.

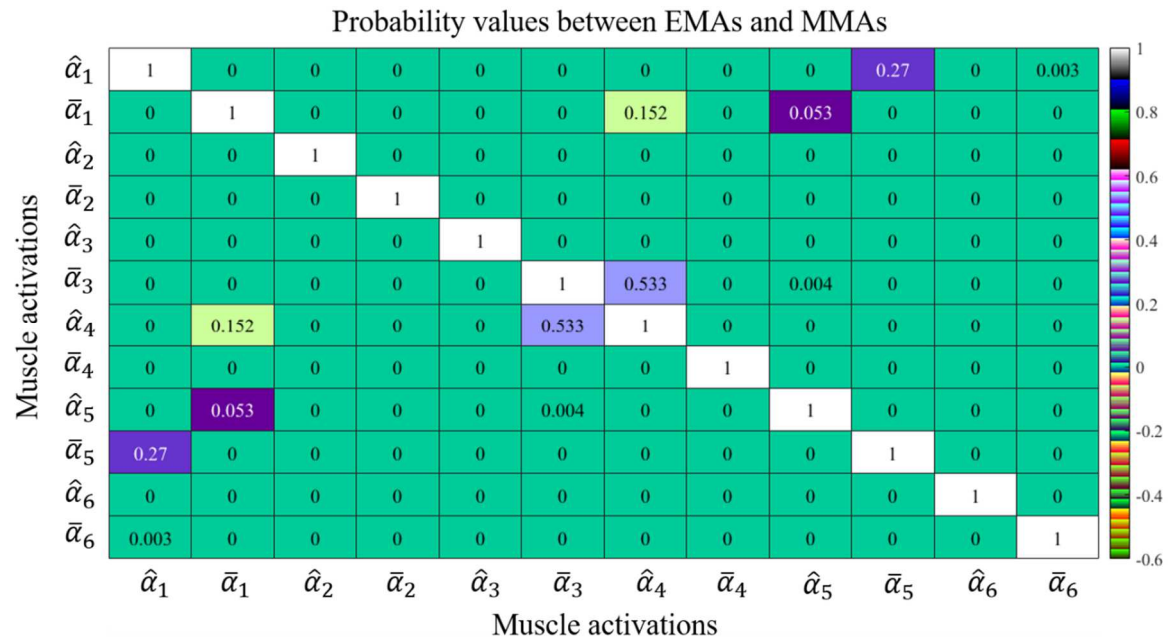
## 4. Discussion

As explained earlier, the proposed controller is in the role of the human CNS, which can generate the required joint torques during the MWP in the sagittal plane. The joint torques are generated by the contraction of the upper limb active muscles during the MWP. This study aims to extract the required muscle activations and analyze the CNS strategy to control upper limb movements for task-specific FES rehabilitation therapy. Furthermore, this is the first study to design the ALFS system for pushrim force measurement, which does not influence the configuration characteristics of MWs, such as weight, etc.





(a)



(b)

Fig. 11. (a) CCs and (b) Pvalues between EMAs and MMAs.

**4.1. Analysis of Pushrim Force**

The current study made the experiment more realistic by considering the slight weight change and the possibility of propulsion on asphalt. All participants used the semicircular pattern for propulsion. In this pattern, the hand moves closer to the pushrim at the end of the recovery phase. The push phase starts with the hand stretched upward and in contact with the pushrim. Therefore, the radial component increased faster than the tangential component in the first half of the push phase, as shown in Fig. 8.

To our knowledge, only a few studies have reported continuous data on pushrim force components. A review study conducted by Halloran et al. [54] revealed that the maximum value of the tangential component fell within the range of 29 N to 108 N, whereas the maximum value of the radial component was between 26 N and 60 N. The reported results consistently indicated that the tangential components displayed a single peak at the end of the push phase, while the radial components exhibited two or more peaks. Additionally, this review study suggests that variations in waveform characteristics can be attributed to differences in propulsion patterns and the velocity of manual wheelchairs. Therefore, the pushrim force components measured by the applied ALFS system, in accordance with propulsion pattern analysis and previous literature, are deemed highly validated.

**4.2. Performance Analysis of Nonlinear Model Predictive Controller**

The implication of the proposed controller to the upper limb MSK model yields favorable outcomes, as demonstrated in Fig. 9, where the measured angular positions are accurately tracked. The results exhibit robustness against uncertainty, high accuracy, ideal transient response, and fast convergence. Notably, despite the presence of uncertainties and external pushrim force, the



control inputs applied to the dynamic model remain desirable and acceptable, as evidenced by the simulation results. The efficiency of the proposed controller is further confirmed by the estimated joint torques, as depicted in Fig. 9.

The depicted control inputs in Fig. 9 represent the joint torques generated at the shoulder and elbow joints, respectively. As expected, the greater weight of the upper arm compared to other segments causes a significantly greater inertial force to be applied to the shoulder joint compared to the elbow. Therefore, active muscles in the shoulder joint contract more than other upper limb muscle groups. The torque curves in the push phase indicate that the maximum estimated torques are observed at 7.9% and 30.3% of the propulsion cycle, respectively. However, this analysis can also be obtained by considering the maximum pushrim force values in the push phase.

Overall, previous studies that investigated the upper limb's kinetics during MWP confirm our study's simulation results. According to their reports, the maximum torques among upper limb joints are related to shoulder extension and elbow extension, respectively. The results of seventeen participants indicated that peak shoulder joint torque was greatest in shoulder extension [68]. They reported a peak shoulder extension torque of 32.5 (12.9) Nm, achieved at a speed of  $1.51 \text{ ms}^{-1}$ . Since the average MW speed in our study is  $1.45 \text{ ms}^{-1}$ , the difference in peak shoulder joint torque between our results and theirs is justified. Agudo et al. [69] found that the significant joint torque corresponded to shoulder extension but with a less absolute value of 7.9 (3.5). The lower absolute value of their results compared to other studies is due to using a treadmill. The treadmill may produce less friction than other devices, such as ergometers [70] and dynamometers [71]. Two studies have reported significant values for peak shoulder extension torques between 42.9 and 52.1 Nm, possibly related to using ergometers to measure kinetics [72, 73]. Other studies [74, 75] have obtained peak shoulder extension torques ranging from 19.6 to 35 Nm. Therefore, our findings are situated within the range of these values. Peak elbow extension torques have been obtained between 10 and 21 Nm [74, 75]. Therefore, our estimated value of 19.1 Nm is within this range. As with the peak shoulder extension torque, Finley et al. [73] reported a significant elbow extension torque with a value of 36.2 (23.2), which is unacceptable due to the maximum voluntary isometric contraction of elbow extensor muscles.

#### 4.3. Performance Analysis of Muscle Optimization

Comparing the obtained CCs between MMAs indicates that CNS classifies the considered muscles as at least two muscle synergies [76], which is drawn from excellent similarity. By considering two synergies, AD, PM, and LBB are co-activated together as a first muscle synergy, while PD, LOTB, and LATB are co-activated together as the second muscle synergy. This classification helps to evaluate the EMAs. Based on the results, comparing the obtained CCs between EMAs of the agonist muscles indicates good similarities between the following muscle pairs:  $(\hat{\alpha}_{AD}, \hat{\alpha}_{PM})$  and  $(\hat{\alpha}_{PM}, \hat{\alpha}_{LBB})$ , although there is a fair similarity between  $\hat{\alpha}_{AD}$  and  $\hat{\alpha}_{LBB}$ . For antagonist muscles, there are good similarities between the following muscle pairs:  $(\hat{\alpha}_{PD}, \hat{\alpha}_{LATB})$  and  $(\hat{\alpha}_{LOTB}, \hat{\alpha}_{LATB})$ , although there is a fair similarity between  $\hat{\alpha}_{PD}$  and  $\hat{\alpha}_{LOTB}$ . Therefore, considering the above acceptable similarities and the lack of any dissimilarities between corresponding EMAs and MMAs, the obtained results from muscle optimization are well validated. Note that the evaluation of CCs between corresponding EMAs and MMAs indicates the lowest correlation between  $\hat{\alpha}_{LBB}$  and  $\bar{\alpha}_{LBB}$ , which is the reason for the decrease in the optimization performance.

#### 4.4. The Strategy of the Central Nervous System to Activate Muscles during Manual Wheelchair Propulsion

In the shoulder joint space, at the beginning of the push phase (from 0 to 22.4%), AD and PM contract to accelerate the upper arm flexion by generating positive torques in the shoulder joint. Since the moment arm of LBB related to the shoulder joint is small in this period, LBB contracts slightly with AD and PM. Then, from 22.4 to 41.4%, PD and LOTB contract significantly to decelerate the upper arm flexion by generating negative torques in the shoulder joint. Note that decreasing the moment arm of the LOTB at the end of this period reduces the generated torque. However, at the first half of the recovery phase (from 35 to 56.3%), since no pushrim force is exerted and the acceleration of gravity affects the extension of the upper arm, the PD contracts slightly. At the last half of the recovery phase (from 56.3 to 100%), PD and LOTB contract significantly to accelerate the upper arm extension by generating negative torque in the shoulder joint.

In the elbow joint space, at the beginning of the push phase (from 0 to 12%), LBB contracts to accelerate the forearm flexion by generating positive torque in the elbow joint. Then, from 12 to 19.7%, LATB and LOTB contract to decelerate the forearm flexion by generating negative torque. Afterward, from 19.7 to 38.7%, these antagonist muscles contract significantly to accelerate the forearm extension by generating negative torque. On the other hand, LBB contracts slightly to decelerate the forearm extension by generating positive torque in the first half of the recovery phase (from 38.7 to 52.7%). For the rest of the recovery phase (from 52.7 to 100%), LBB has a significant contraction to accelerate the forearm flexion by generating positive torque. Note that the extensor muscles of the elbow joint (LATB and LOTB) contract in the last half of the recovery phase to control the acceleration of the forearm and thus to track the measured trajectory during forearm flexion.

## 5. Conclusion

The human anatomy is characterized by a high level of redundancy, which requires implementing optimal criteria for body movements, such as MWP. To this aim, an optimal controller is applied to the two DOFs MSK model of the upper arm, including six muscles, to simulate the repetitive movements of the upper arm during MWP. Results indicate that the proposed controller can effectively control the MSK model by generating optimal joint torques within the range of joint physiology [77]. Developing the MSK model considering the gravity and external forces, the possibility of considering constraints in the control structure, using the NMPC to estimate optimal joint torques based on the future predictive horizon, using a more robust optimization strategy in dealing with nonlinear dynamics than the CMC, are some of the advantages of this study, which led to the fulfillment of the research objectives, i.e., generating the optimal low-intensity electrical signals and accurately tracking the angular positions in the joint space. Future work will focus on applying the current study for task-specific FES rehabilitation therapy.

## 6. Study Limitations

The current investigation has some limitations that need to be explained. Firstly, none of the participants had upper limb pain, injuries, or disorders, whereas this study seeks to understand the CNS strategy to account for biomechanical considerations aimed at reducing joint injuries. Therefore, since the influence of impaired motor control ability of MWUs are not visible in our simulation results, this study is only to understand the mechanism of injury, analyze CNS function, and consider rehabilitation guidelines for new users and people without motor disability. Furthermore, healthy participants adapt more quickly to the constraints of experimental items. Secondly, all participants were right upper limb dominant; therefore, the required dataset was recorded only from their right upper limb segments. Generally, the assumption of bilateral symmetry during MWP for studies that analyze groups of participants without significant upper limb pain or impairment is supported in previous studies [78], whereas small asymmetries



are reported for more strenuous conditions. Therefore, it would be better to record bilateral data for the MWP on the incline surface, which imposes a high muscular demand on the upper limb. Note that the propelling in a straight line, considered in the procedure, can also confirm this assumption. Thirdly, the test ground surface was considered asphalt, which has high friction coefficient [79], because long-term manual wheelchair propulsion mostly occurs outdoors. Therefore, it is better to distinguish between MWP on different surfaces for the design of rehabilitation guidelines because the results of this study can be relied upon just for asphalt surfaces. Note that the friction between the rubber and the surface also depends on some factors, such as longitudinal wheelchair speed and slip [79]. Finally, although various propulsion patterns are used by MWUs [80], all participants only utilized the semicircular pattern as the most effective propulsion pattern [50]. Each pattern has different biomechanical characteristics that can change the results of the research [80]. Therefore, muscle synergy, as a sensitive biomedical indicator, definitely has a different level of activation compared to different patterns.

### Author Contributions

M.M. Rusta and S.A. Haghpanah planned the scheme, initiated the project, suggested the experiments, conducted the experiments and analyzed the empirical results, developed the mathematical modeling and examined the theory validation. The manuscript was written through the contribution of all authors. All authors discussed the results, reviewed, and approved the final version of the manuscript.

### Acknowledgments

The authors are grateful to Dr. Eftekhari for fruitful discussions and advice.

### Conflict of Interest

The authors declared no potential conflicts of interest concerning the research, authorship, and publication of this article.

### Funding

The authors received no financial support for the research, authorship, and publication of this article.

### Data Availability Statements

The datasets generated and/or analyzed during the current study are available from the corresponding author on reasonable request.

### Nomenclature

$L_i$	Length of segment	$M$	Inertia matrix
$d_i$	Mass center position of segment	$C$	Coriolis and centrifugal and friction torque matrix
$m_i$	Mass of segment	$G$	Gravity vector
$\theta_i$	Angular position of joint	$\tau$	Vector of external torques
$\dot{\theta}_i$	Angular velocity of joint	$R_T$	Vector of pushrim force components
$l_i$	Length of muscle	$\mathcal{F}_{IT}$	Objective function in NMPC
$\dot{l}_i$	Muscle contractile velocity	$\mathcal{F}_{MF}$	Objective function in muscle optimization
$\ddot{a}_i$	Attachment point of AD	$\hat{\theta}$	Estimated angular position
$\ddot{b}_i$	Attachment point of PD	$\bar{\theta}$	Measured angular position
$\ddot{c}_i$	Attachment point of PM	$\hat{T}$	Estimated joint torque
$\ddot{d}_i$	Attachment point of LBB	$it$	Iteration number in the Levenberg-Marquardt method
$\ddot{e}_i$	Attachment point of LOTB	$D$	Search direction in the Levenberg-Marquardt method
$\ddot{f}_i$	Attachment point of LATB	$\lambda_m$	Control parameter for D in the Levenberg-Marquardt method
$W^T$	Jacobian matrix between contractile velocity of muscles and angular velocity of joints	$\Psi(\hat{T})$	Vector of errors considering prediction horizon in the Levenberg-Marquardt method
$f$	Muscle tensile force	$\Gamma$	Jacobian matrix of $\Psi(\hat{T})$
$T$	Joint torque	$\Omega$	Modification operator in the Levenberg-Marquardt method
$c_0$	Muscle intrinsic viscosity	$\varepsilon$	Optimality tolerance value in Levenberg-Marquardt method
$\alpha_c$	muscle control input	$lb$	Lower bound of joint torque
$f_0$	Maximum muscle force in Hill model	$ub$	Upper bound of joint torque
$\dot{X}$	Vector of end-point linear velocities	$\sigma_{max}$	Maximum allowable muscle stress
$J$	Jacobian matrix from the task space to the joint space	$PCSA$	Physiological cross-sectional area
$L$	Lagrangian	$\hat{\alpha}$	Estimated muscle activation
$E_k$	Kinetic energy	$\bar{\alpha}$	Measured muscle activation
$E_p$	Potential energy	$r$	Pearson's correlation coefficient
$Q_{nc}$	Non-conservative forces	$p$	Probability value

### References

- [1] Gurwitz, J.H., Carlozzi, N.E., Davison, K.K., Evenson, K.R., Gaskin, D.J., Lushniak, B., National Institutes of health pathways to prevention workshop: physical activity and health for wheelchair users, *Archives of Rehabilitation Research and Clinical Translation*, 3, 2021, 100163.
- [2] Curi, H.T., Lima, J.D., Ferretti, E.C., Factors related to propulsion efficiency in manual wheelchair users with paraplegia due to spinal cord injury, *Cadernos Brasileiros de Terapia Ocupacional*, 28, 2020, 999-1019.
- [3] Finley, M.A., Euiler, E., Association of musculoskeletal pain, fear-avoidance factors, and quality of life in active manual wheelchair users with SCI: A pilot study, *The Journal of Spinal cord Medicine*, 43, 2020, 497-504.
- [4] Divanoglou, A., Augutis, M., Sveinsson, T., Hultling, C., Levi, R., Self-reported health problems and prioritized goals in community-dwelling



individuals with spinal cord injury in Sweden, *Journal of Rehabilitation Medicine*, 50, 2018.

- [5] Mercer, J.L., Boninger, M., Koontz, A., Ren, D., Dyson-Hudson, T., Cooper, R., Shoulder joint kinetics and pathology in manual wheelchair users, *Clinical Biomechanics*, 21, 2006, 781-789.
- [6] Zamarioli, A., Gene expression and bone loss following spinal cord injury, In *Cellular, Molecular, Physiological, and Behavioral Aspects of Spinal Cord Injury*, Academic Press, 2022, 81-92.
- [7] Vives Alvarado, J.R., Felix, E.R., Gater Jr, D.R., Upper extremity overuse injuries and obesity after spinal cord injury, *Topics in Spinal Cord Injury Rehabilitation*, 27, 2021, 68-74.
- [8] Kesar, T.M., Perumal, R., Reisman, D.S., Jancosko, A., Rudolph, K.S., Higginson, J.S., Binder-Macleod, S.A., Functional electrical stimulation of ankle plantarflexor and dorsiflexor muscles: effects on poststroke gait, *Stroke*, 40, 2009, 3821-3827.
- [9] Khalid, S., Alnajjar, F., Gochoo, M., Renawi, A., Shimoda, S., Robotic assistive and rehabilitation devices leading to motor recovery in upper limb: a systematic review, *Disability and Rehabilitation: Assistive Technology*, 18, 2023, 658-672.
- [10] Yildiz, I., A low-cost and lightweight alternative to rehabilitation robots: omnidirectional interactive mobile robot for arm rehabilitation, *Arabian Journal for Science and Engineering*, 43, 2018, 1053-1059.
- [11] Page, S.J., Levine, P., Leonard, A., Szaflarski, J.P., Kissela, B.M., Modified constraint-induced therapy in chronic stroke: results of a single-blinded randomized controlled trial, *Physical Therapy*, 88, 2008, 333-340.
- [12] Laver, K.E., Lange, B., George, S., Deutsch, J.E., Saposnik, G., Crotty, M., Virtual reality for stroke rehabilitation, *Cochrane Database of Systematic Reviews*, 11, 2017.
- [13] Latreche, A., Kelaiaia, R., Chemori, A., Kerboua, A., A New Home-Based Upper-and Lower-Limb Telerehabilitation Platform with Experimental Validation, *Arabian Journal for Science and Engineering*, 2023, 1-16.
- [14] Latreche, A., Kelaiaia, R., Chemori, A., Kerboua, A., Reliability and validity analysis of MediaPipe-based measurement system for some human rehabilitation motions, *Measurement*, 214, 2023, 112826.
- [15] Marquez-Chin, C., Popovic, M.R., Functional electrical stimulation therapy for restoration of motor function after spinal cord injury and stroke: a review, *Biomedical Engineering Online*, 19, 2020, 1-25.
- [16] Rushton, D.N., Functional electrical stimulation, *Physiological Measurement*, 18, 1997, 241.
- [17] Freeman, C.T., Hughes, A.M., Burridge, J.H., Chappell, P.H., Lewin, P.L., Rogers, E., A model of the upper extremity using FES for stroke rehabilitation, *The Journal of Biomechanical Engineering*, 131, 2009, 1-12.
- [18] Alashram, A.R., Annino, G., Mercuri, N.B., Changes in spasticity following functional electrical stimulation cycling in patients with spinal cord injury: A systematic review, *The Journal of Spinal Cord Medicine*, 45, 2022, 10-23.
- [19] Popovic, D.B., Advances in functional electrical stimulation (FES), *Journal of Electromyography and Kinesiology*, 24, 2014, 795-802.
- [20] Ferrante, S., Chia Bejarano, N., Ambrosini, E., Nardone, A., Turcato, A.M., Monticone, M., Ferrigno, G., Pedrocchi, A., A personalized multi-channel FES controller based on muscle synergies to support gait rehabilitation after stroke, *Frontiers in Neuroscience*, 10, 2016, 425.
- [21] Hodkin, E.F., Lei, Y., Humby, J., Glover, I.S., Choudhury, S., Kumar, H., Perez, M.A., Rodgers, H., Jackson, A., Automated FES for upper limb rehabilitation following stroke and spinal cord injury, *IEEE Transactions on Neural Systems and Rehabilitation Engineering*, 26, 2018, 1067-1074.
- [22] Cheung, V.C., Niu, C.M., Li, S., Xie, Q., Lan, N., A novel FES strategy for poststroke rehabilitation based on the natural organization of neuromuscular control, *IEEE Reviews in Biomedical Engineering*, 12, 2018, 154-167.
- [23] Uno, Y., Kawato, M., Suzuki, R., Formation and control of optimal trajectory in human multijoint arm movement, *Biological Cybernetics*, 61, 1989, 89-101.
- [24] Jagodnik, K.M., Van den Bogert, A.J., Optimization and evaluation of a proportional derivative controller for planar arm movement, *Journal of Biomechanics*, 43, 2010, 1086-1091.
- [25] Zadavec, M., Matjačić, Z., Planar arm movement trajectory formation: an optimization based simulation study, *Biocybernetics and Biomedical Engineering*, 33, 2013, 106-117.
- [26] Sharifi, M., Salarieh, H., Behzadipour, S., Nonlinear optimal control of planar musculoskeletal arm model with minimum muscles stress criterion, *Journal of Computational and Nonlinear Dynamics*, 12, 2017, 011014.
- [27] Ghannadi, B., Sharif Razavian, R., McPhee, J., Configuration-dependent optimal impedance control of an upper extremity stroke rehabilitation manipulandum, *Frontiers in Robotics and AI*, 5, 2018, 124.
- [28] Wu, Y., Chen, J., Qiao, H., Anti-interference analysis of bio-inspired musculoskeletal robotic system, *Neurocomputing*, 436, 2021, 114-125.
- [29] Ghorbani, H., Vatankhah, R., Haghpanah, S.A., Zolotash, S., Musculoskeletal Modeling and Simulation of the Human Arm in Rehabilitation by Shoulder Wheel Device Using an Adaptive Robust Control Scheme, *Iranian Journal of Science and Technology, Transactions of Mechanical Engineering*, 46, 2022, 1067-1078.
- [30] Zhao, Y., Zhang, M., Wu, H., He, X., Todoh, M., Neuromechanics-Based Neural Feedback Controller for Planar Arm Reaching Movements, *Bioengineering*, 10, 2023, 436.
- [31] Tahara, K., Kino, H., Reaching movements of a redundant musculoskeletal arm: Acquisition of an adequate internal force by iterative learning and its evaluation through a dynamic damping ellipsoid, *Advanced Robotics*, 24, 2010, 783-818.
- [32] Tahara, K., Kuboyama, Y., Kurazume, R., Iterative learning control for a musculoskeletal arm: Utilizing multiple space variables to improve the robustness, *IEEE/RSJ International Conference on Intelligent Robots and Systems*, 2012, 4620-4625.
- [33] Wang, T., Song, A., Adaptive neural fuzzy inference system disturbance observer-based control for reaching movement of musculoskeletal arm model, *IEEE Access*, 6, 2018, 73030-73040.
- [34] Vatankhah, R., Broushaki, M., Alasty, A., Adaptive optimal multi-critic based neuro-fuzzy control of MIMO human musculoskeletal arm model, *Neurocomputing*, 173, 2016, 1529-1537.
- [35] Xiuxiang, C., Ting, W., Yongkun, Z., Wen, Q., Xinghua, Z., An adaptive fuzzy sliding mode control for angle tracking of human musculoskeletal arm model, *Computers & Electrical Engineering*, 72, 2018, 214-223.
- [36] Roelker, S.A., Caruthers, E.J., Baker, R.K., Pelz, N.C., Chaudhari, A.M., Siston, R.A., Interpreting musculoskeletal models and dynamic simulations: causes and effects of differences between models, *Annals of Biomedical Engineering*, 45, 2017, 2635-2647.
- [37] Kainz, H., Modenese, L., Lloyd, D.G., Maine, S., Walsh, H.P.J., Carty, C.P., Joint kinematic calculation based on clinical direct kinematic versus inverse kinematic gait models, *Journal of Biomechanics*, 49, 2016, 1658-1669.
- [38] Myers, C.A., Laz, P.J., Shelburne, K.B., Davidson, B.S., A probabilistic approach to quantify the impact of uncertainty propagation in musculoskeletal simulations, *Annals of Biomedical Engineering*, 2015, 43:1098-111.
- [39] Anderson, F.C., Pandy, M.G., Dynamic optimization of human walking, *The Journal of Biomechanical Engineering*, 123, 2001, 381-390.
- [40] Thelen, D.G., Anderson, F.C., Using computed muscle control to generate forward dynamic simulations of human walking from experimental data, *Journal of Biomechanics*, 39, 2006, 1107-1115.
- [41] De Groot, F., Demeulenaere, B., Swevers, J., De Schutter, J., Jonkers, I., A physiology-based inverse dynamic analysis of human gait using sequential convex programming: a comparative study, *Computer Methods in Biomechanics and Biomedical Engineering*, 15, 2012, 1093-1102.
- [42] Wesseling, M., De Groot, F., Jonkers, I., The effect of perturbing body segment parameters on calculated joint moments and muscle forces during gait, *Journal of Biomechanics*, 47, 2014, 596-601.
- [43] Wesseling, M., Derikx, L.C., De Groot, F., Bartels, W., Meyer, C., Verdonschot, N., Jonkers, I., Muscle optimization techniques impact the magnitude of calculated hip joint contact forces, *Journal of Orthopaedic Research*, 33, 2015, 430-438.
- [44] Rankin, J.W., Rubenson, J., Hutchinson, J.R., Inferring muscle functional roles of the ostrich pelvic limb during walking and running using computer optimization, *Journal of the Royal Society Interface*, 13, 2016, 20160035.
- [45] Lin, Y.C., Dorn, T.W., Schache, A.G., Pandy, M.G., Comparison of different methods for estimating muscle forces in human movement, *Proceedings of the Institution of Mechanical Engineers, Part H: Journal of Engineering in Medicine*, 226, 2012, 103-112.
- [46] Mokhtarzadeh, H., Perraton, L., Fok, L., Muñoz, M.A., Clark, R., Pivonka, P., Bryant, A.L., A comparison of optimisation methods and knee joint degrees of freedom on muscle force predictions during single-leg hop landings, *Journal of Biomechanics*, 47, 2014, 2863-2868.
- [47] Grüne, L., Pannek, J., *Nonlinear model predictive control*, Springer International Publishing, 2017, 45-69.
- [48] Levenberg, K., A method for the solution of certain non-linear problems in least squares, *Quarterly of Applied Mathematics*, 2, 1944, 164-168.
- [49] Altman, A. and Gondzio, J., Regularized symmetric indefinite systems in interior point methods for linear and quadratic optimization, *Optimization*



Methods and Software, 11, 1999, 275-302.

- [50] Slowik, J.S., Requejo, P.S., Mulroy, S.J., Neptune, R.R., The influence of wheelchair propulsion hand pattern on upper extremity muscle power and stress, *Journal of Biomechanics*, 49, 2016, 1554-1561.
- [51] Hermens, H.J., Freriks, B., Disselhorst-Klug, C., Rau, G., Development of recommendations for SEMG sensors and sensor placement procedures, *Journal of Electromyography and Kinesiology*, 10, 2000, 361-374.
- [52] Padulo, J., Vando, S., Chamari, K., Chaouachi, A., Bagno, D., Pizzolato, F., Validity of the MarkWiir for kinematic analysis during walking and running gaits, *Biology of Sport*, 32, 2015, 53-58.
- [53] Ugbohue, U.C., Papi, E., Kaliarntas, K.T., Kerr, A., Earl, L., Pomeroy, V.M., Rowe, P.J., The evaluation of an inexpensive, 2D, video based gait assessment system for clinical use, *Gait & Posture*, 38, 2013, 483-489.
- [54] Halloran, K., Focht, M., Teague, A., Peters, J., Rice, I., Kersh, M., Moving forward: A review of continuous kinetics and kinematics during wheelchair and handcycling propulsion, *Journal of Biomechanics*, 159, 2023, 111779.
- [55] Hajiloo, B., Anbarian, M., Esmaeili, H., Mirzapour, M., The effects of fatigue on synergy of selected lower limb muscles during running, *Journal of Biomechanics*, 103, 2020, 109692.
- [56] Turpin, N.A., Uriac, S., Dalleau, G., How to improve the muscle synergy analysis methodology?, *European Journal of Applied Physiology*, 121, 2021, 1009-1025.
- [57] Cooper, R.A., DiGiovine, C.P., Boninger, M.L., Shimada, S.D., Koontz, A.M., Baldwin, M.A., Filter frequency selection for manual wheelchair biomechanics, *Journal of Rehabilitation Research & Development*, 39, 2002, 323-336.
- [58] Mulroy, S.J., Gronley, J.K., Newsam, C.J., Perry, J., Electromyographic activity of shoulder muscles during wheelchair propulsion by paraplegic persons, *Archives of Physical Medicine and Rehabilitation*, 77, 1996, 187-193.
- [59] Cerquiglini, S., Figura, F., Marchetti, M., Ricci, B., Biomechanics of wheelchair propulsion, In *Biomechanics VII-A*, Park Press, 1981, 410-419.
- [60] Winter, D.A., *Biomechanics and motor control of human movement*, John Wiley & Sons, 2009.
- [61] Holzbaaur, K.R., Murray, W.M., Gold, G.E., Delp, S.L., Upper limb muscle volumes in adult subjects, *Journal of Biomechanics*, 40, 2007, 742-749.
- [62] Murray, W.M., Buchanan, T.S., Delp, S.L., The isometric functional capacity of muscles that cross the elbow, *Journal of Biomechanics*, 33, 2000, 943-952.
- [63] Veeger, H.E.J., Yu, B., An, K.N., Rozendal, R.H., Parameters for modeling the upper extremity, *Journal of Biomechanics*, 30, 1997, 647-652.
- [64] Pigeon, P. and Feldman, A.G., Moment arms and lengths of human upper limb muscles as functions of joint angles, *Journal of Biomechanics*, 29, 1996, 1365-1370.
- [65] Tahara, K., Arimoto, S., Sekimoto, M., Luo, Z.W., On control of reaching movements for musculo-skeletal redundant arm model, *Applied Bionics and Biomechanics*, 6, 2009, 11-26.
- [66] Marquardt, D.W., An algorithm for least-squares estimation of nonlinear parameters, *Journal of the Society for Industrial and Applied Mathematics*, 11, 1963, 431-441.
- [67] Chvatal, S.A., Ting, L.H., Voluntary and reactive recruitment of locomotor muscle synergies during perturbed walking, *Journal of Neuroscience*, 32, 2012, 12237-12250.
- [68] Kulig, K., Rao, S.S., Mulroy, S.J., Newsam, C.J., Gronley, J.K., Bontrager, E.L., Perry, J., Shoulder joint kinetics during the push phase of wheelchair propulsion, *Clinical Orthopaedics and Related Research*, 354, 1998, 132-143.
- [69] Gil-Agudo, A., Ama-Espinosa, D., Pérez-Rizo, E., Pérez-Nombela, S., Crespo-Ruiz, B., Shoulder joint kinetics during wheelchair propulsion on a treadmill at two different speeds in spinal cord injury patients, *Spinal Cord*, 48, 2010, 290-296.
- [70] Veeger, H.E.J., Rozendaal, L.A., Van der Helm, F.C.T., Load on the shoulder in low intensity wheelchair propulsion, *Clinical Biomechanics*, 17, 2002, 211-218.
- [71] Collinger, J.L., Boninger, M.L., Koontz, A.M., Price, R., Sisto, S.A., Tolerico, M.L., Cooper, R.A., Shoulder biomechanics during the push phase of wheelchair propulsion: a multisite study of persons with paraplegia, *Archives of Physical Medicine and Rehabilitation*, 89, 2008, 667-676.
- [72] Cooper, R.A., Boninger, M.L., Shimada, S.D., Lawrence, B.M., Glenohumeral joint kinematics and kinetics for three coordinate system representations during wheelchair propulsion, *American Journal of Physical Medicine & Rehabilitation*, 78, 1999, 435-446.
- [73] Finley, M.A., Rasch, E.K., Keyser, R.E., Rodgers, M.M., The biomechanics of wheelchair propulsion in individuals with and without upper-limb impairment, *Journal of Rehabilitation Research & Development*, 41, 2004, 385-395.
- [74] Robertson, R.N., Boninger, M.L., Cooper, R.A., Shimada, S.D., Pushrim forces and joint kinetics during wheelchair propulsion, *Archives of Physical Medicine and Rehabilitation*, 77, 1996, 856-864.
- [75] Veeger, H.E.J., Van Der Woude, L.H.V., Rozendal, R.H., Load on the upper extremity in manual wheelchair propulsion, *Journal of Electromyography and Kinesiology*, 1, 1991, 270-280.
- [76] Latash M., On primitives in motor control, *Motor Control*, 24, 2020, 318-46.
- [77] Sabick, M.B., Kotajarvi, B.R., An, K.N., A new method to quantify demand on the upper extremity during manual wheelchair propulsion, *Archives of Physical Medicine and Rehabilitation*, 85, 2004, 1151-1159.
- [78] Soltau, S.L., Slowik, J.S., Requejo, P.S., Mulroy, S.J., Neptune, R.R., An investigation of bilateral symmetry during manual wheelchair propulsion, *Frontiers in Bioengineering and Biotechnology*, 3, 2015, 86.
- [79] Lex, C., Maximum tire-road friction coefficient estimation, Verlag der Techn. Univ. Graz, 2015. <https://openlib.tugraz.at/download.php?id=565316e131a71&location=browse>.
- [80] Walford, S.L., Rankin, J.W., Mulroy, S.J., Neptune, R.R., The relationship between the hand pattern used during fast wheelchair propulsion and shoulder pain development, *Journal of Biomechanics*, 116, 2021, 110202.

## Appendix A

As stated in the kinetics section, the dynamic equation of the two DOFs upper limb model in the sagittal plane is defined as follows:

$$\{\mathbf{Q}_{n.c}\}_{2 \times 1} = [\mathbf{M}(\boldsymbol{\theta})]_{2 \times 2} \{\ddot{\boldsymbol{\theta}}\}_{2 \times 1} + [\mathbf{C}(\boldsymbol{\theta}, \dot{\boldsymbol{\theta}})]_{2 \times 2} \{\dot{\boldsymbol{\theta}}\}_{2 \times 1} + \{\mathbf{G}(\boldsymbol{\theta})\}_{2 \times 1} \quad (\text{A.1})$$

where  $[\mathbf{M}(\boldsymbol{\theta})] \in \mathbb{R}^{2 \times 2}$  means the inertia matrix, which is defined as follows:

$$[\mathbf{M}(\boldsymbol{\theta})]_{2 \times 2} = \begin{pmatrix} m_{11} & m_{12} \\ m_{21} & m_{22} \end{pmatrix} \quad (\text{A.2})$$

where its arrays are:

$$m_{11} = I_1 + I_2 + L_1^2 m_2 + d_1^2 m_1 + d_2^2 m_2 + 2L_1 d_2 m_2 \cos(\theta_2) \quad (\text{A.3})$$

$$m_{12} = I_2 + m_2 d_2^2 + L_1 d_2 m_2 \cos(\theta_2) \quad (\text{A.4})$$

$$m_{21} = m_{12} \quad (\text{A.5})$$



$$m_{22} = I_2 + m_2 d_2^2 \quad (\text{A.6})$$

and  $[C(\theta, \dot{\theta})] \in \mathbb{R}^{2 \times 2}$  means the Coriolis and centrifugal matrix, which is defined as follows:

$$[C(\theta, \dot{\theta})]_{2 \times 2} = \begin{pmatrix} c_{11} & c_{12} \\ c_{21} & c_{22} \end{pmatrix} \quad (\text{A.7})$$

where its arrays are:

$$c_{11} = -L_1 d_2 m_2 \dot{\theta}_2 \sin(\theta_2) \quad (\text{A.8})$$

$$c_{12} = -L_1 d_2 m_2 \sin(\theta_2) (\dot{\theta}_1 + \dot{\theta}_2) \quad (\text{A.9})$$

$$c_{21} = L_1 d_2 m_2 \dot{\theta}_1 \sin(\theta_2) \quad (\text{A.10})$$

$$c_{22} = 0 \quad (\text{A.11})$$

and  $\{G(\theta)\} \in \mathbb{R}^2$  means the gravity vector, which is defined as follows:

$$\{G(\theta)\}_{2 \times 1} = (g_1 \quad g_2)^T \quad (\text{A.12})$$

where its arrays are:

$$g_1 = gm_2(d_2 \sin(\theta_1 + \theta_2) + L_1 \sin(\theta_1)) + gd_1 m_1 \sin(\theta_1) \quad (\text{A.13})$$

$$g_2 = gd_2 m_2 \sin(\theta_1 + \theta_2) \quad (\text{A.14})$$

## ORCID iD

Mohammad Mahdi Rusta  <https://orcid.org/0000-0003-1241-3294>

Seyyed Arash Haghpanah  <https://orcid.org/0000-0002-3121-0161>

Sajjad Taghvaei  <https://orcid.org/0000-0002-2266-2449>



© 2023 Shahid Chamran University of Ahvaz, Ahvaz, Iran. This article is an open access article distributed under the terms and conditions of the Creative Commons Attribution-NonCommercial 4.0 International (CC BY-NC 4.0 license) (<http://creativecommons.org/licenses/by-nc/4.0/>).

**How to cite this article:** Rusta M.M., Haghpanah S.A., Taghvaei S. Musculoskeletal Modeling and Control of the Human Upper Limb during Manual Wheelchair Propulsion: Application in Functional Electrical Stimulation Rehabilitation Therapy, *J. Appl. Comput. Mech.*, 10(1), 2024, 92–110. <https://doi.org/10.22055/jacm.2023.44469.4217>

**Publisher's Note** Shahid Chamran University of Ahvaz remains neutral with regard to jurisdictional claims in published maps and institutional affiliations.

